LIÈGE université Library

https://lib.uliege.be

https://matheo.uliege.be

Final thesis

Auteur : Vander Donckt, Mathieu
Promoteur(s) : Jehin, Emmanuel
Faculté : Faculté des Sciences
Diplôme : Master de spécialisation en cosmos exploration
Année académique : 2020-2021
URI/URL : http://hdl.handle.net/2268.2/12716

Avertissement à l'attention des usagers :

Tous les documents placés en accès ouvert sur le site le site MatheO sont protégés par le droit d'auteur. Conformément aux principes énoncés par la "Budapest Open Access Initiative"(BOAI, 2002), l'utilisateur du site peut lire, télécharger, copier, transmettre, imprimer, chercher ou faire un lien vers le texte intégral de ces documents, les disséquer pour les indexer, s'en servir de données pour un logiciel, ou s'en servir à toute autre fin légale (ou prévue par la réglementation relative au droit d'auteur). Toute utilisation du document à des fins commerciales est strictement interdite.

Par ailleurs, l'utilisateur s'engage à respecter les droits moraux de l'auteur, principalement le droit à l'intégrité de l'oeuvre et le droit de paternité et ce dans toute utilisation que l'utilisateur entreprend. Ainsi, à titre d'exemple, lorsqu'il reproduira un document par extrait ou dans son intégralité, l'utilisateur citera de manière complète les sources telles que mentionnées ci-dessus. Toute utilisation non explicitement autorisée ci-avant (telle que par exemple, la modification du document ou son résumé) nécessite l'autorisation préalable et expresse des auteurs ou de leurs ayants droit.

University of Liège
Faculty of Sciences
Department of Astrophysics,
Geophysics and Oceanography

PISCO: a Pipeline for the Infrared Spectroscopy of COmets

Application to VLT/CRIRES observations of comet 8P/Tuttle

by

Mathieu Vander Donckt

Supervisor: Pr. Emmanuel Jehin
Co-Supervisor: Dr. Manuela Lippi

Examining Board: Dr. Bertrand Bonfond
Dr. Valérie Van Grootel
Dr. Damien Hutsemékers
Dr. Francisco Pozuelos

Master thesis submitted in partial fulfillment of the requirements for the degree of Master in Cosmos Exploration

Academic year 2020-2021

Contents

Acknowledgment

A lot of my gratitude goes to Pr. Emmanuel Jehin and Dr. Manuela Lippi. Although we did not exactly developed the project we intended to do in the first place, I learned a lot (and had some fun as well) with this one, and I hope the initial plans are just postponed. You were always available to answer my questions, especially in those last days, and to share your expertise. More importantly, I grew more curious about comets and their mysteries. Thank you for supervising me.

I also would like to thank the teachers of the Master in Cosmos Exploration for they have always been open minded, especially during my first year when I was the only student, but I think logistically complicated. Pr. De Becker, I don't know if you remember but I contacted you for the first time 7 years ago, and came back to you more than once; you have always been available to discuss my projects. Thank you.

To my parents and family, for they supported me in many ways during my studies.

Max, thanks for the laugh we had in between our writings. Congratulation on submitting you master thesis.

To Volodia, for your support, and because you should really make a come back to the master thesis business with me.

To the deadline, because I beat you again.

List of abbreviations

CRIRES CRyogenic Infrared Echelle Spectrograph

ESO European Southern Observatory

IR Infrared

JFC Jupiter Family Comet

PISCO Pipeline for the Infrared Spectroscopy of COmets

PSG Planetary Spectrum Generator

S/N Signal over Noise

1 Introduction

Comets are among the most spectacular objects one can admire in the sky. Made of ice and dust, they visit us from the fringe of the solar system. The great majority of them are trans-Neptunian objects, spending most of their lifetime in the Kuiper Belt or Oort cloud reservoirs beyond the orbit of Neptune. If a change in their orbit brings them to the inner solar system, their surface ices will sublimate as a result of the increasing solar radiation field, releasing gas and dust, forming the coma. Molecules directly released in the coma from the sublimation of ices are called parent (or primary) molecules, while species that were processed in the coma, notably from photolysis by the Sun radiations, are called daughter (or secondary) species. Comets were formed in the early days of the solar system at the same time as the planets, 4.6 billion years ago. But after their formation, unlike the planets, further away from the Sun and with no internal activity giving them heat, they kept the original chemical composition they had when they formed. It makes them pristine fossils of the solar system and thus their study opens a window into the solar system History. The coma can be studied from ground observatories, while to directly study the nucleus, it is necessary to send a space probe. Successful space missions to comets like Rosetta rendezvous with 67P/Churyumov–Gerasimenko in 2014 greatly improves our understanding of those objects.

This work focuses on the development and testing (with a 8P/Tuttle comet VLT/CRIRES dataset) of the Pipeline for the Infrared Spectroscopy of COmets (PISCO), an integrated compilation of tools and home-made scripts aimed to efficiently and entirely process IR comet observations, from raw images to yielding the production rates. This work is part of a starting effort from the Comet group of the STAR Institute of the University of Liège to develop IR spectroscopy capabilities. The Comet group is already expert in UV-Vis spectroscopy, using the VLT/UVES spectrograph as well as the TRAPPIST telescopes for UV-Vis comet observations. Developing IR capabilities in the group is mainly motivated by two reasons: (a) European institutions are developing the most advanced ground observatories IR spectrographs (VLT/CRIRES+ and ELT/METIS) while the expertise in Europe on IR spectroscopy of comets is almost nonexistent and (b) it will allow for joint observation campaigns of both the parent species (detectable in the IR) and daughter species (detectable in the UV-Vis), which is not commonly done but needed to better understand the overall chemistry of the coma and by extension of the nucleus.

This work is organised as follows:

Section 2 is an introduction to comets. How they were considered in the past, what we know about them today, and what they may hold for us in the future. Multi-wavelength

spectroscopy of comets is also briefly discussed.

Section 3 is concerned with the theory of infrared spectroscopy and some practical considerations like telluric absorptions and the Doppler shift. A description of CRIRES and its successor CRIRES+ is also given. Even though emphasis is given to the complementarity of IR and UV-Vis observations as a context for this work, this work focuses on developing IR capabilities and therefore UV-Vis techniques are not further developed.

Section 4 and Section 5 contain the main original work of this master thesis. Section 4 describes the development and functionalities of PISCO, while Section 5 presents the processing with PISCO of a CRIRES observation of 8P/Tuttle during its 2007-2008 approach.

2 Comets

2.1 A brief History of comets

2.1.1 Fire in the sky: Antiquity and Middle Ages

For thousands of years, comets have inspired awe across human civilisations from their fierce and unpredictable nature. Before the European Renaissance in the 16th century, they were not clearly considered as astronomical objects but rather as heavenly omens or atmospheric phenomenons (Festou, Keller, and Weaver 2004). The earliest known comet observation dates from the 11th century B.C., as reported in an ancient Chinese astronomical record written in the 2nd century B.C. (Ho 1962):

> *When King Wu-Wang waged a punitive war against King Chou a (hui) comet appeared with its tail pointing towards the people of Yin.* (Translated by Ho 1962 from the *Huai Nan Tzu* 15/6b.)

The way the account of the observation is written is interestingly analogous to the astrological nature of comets Ptolemy (100-175 A.D) would conceptualize in Alexandria, a few centuries later. The report of the comet is associated with a destructive event, in this case a war. The comet tail was also used to refer to a place, in this case the land of the people of Yin, that in Ptolemy's view is related to the omen delivered by the comet (although no clear prediction is made in the *Huai Nan Tzu* 15/6b account).

Ptolemy ideas had a great influence on astronomers until the Renaissance, notably with his *epicycles* model of the heavens written in his treaty *Almagest* that scientifically describes the heavenly bodies. He had a less scientific view on the comets, presumably because they were unusual phenomena, and consider them into his other treaty the *Tetrabiblos* that discusses astrology and the influence of heavenly bodies on earthly matter (Yeomans 1991). He described how the comet shape and position could be used to predict the time and the nature of an evil event, while the first apparition and the direction of the tail could be used to predict its location. The *Tetrabiblos* would inspire other astrological works on the interpretation of comets during the Middle Ages.

Ptolemy may have been influenced by the Roman Pliny the Elder (23-79 A.D) that associated comets with disastrous or divine events. Pliny the Elder regarded comets has mysterious signs that would bring discord among men and give rise to wars and other evil events. He namely wrote about probably the most famous comet of the Antiquity, the comet of 44 B.C., that appeared during the games given in the honour of the assassinated Julius Caesar and was interpreted by the people as Julius Caesar soul joining the immortal gods.

The apparition of the 44 B.C. comet is interesting for its societal impact, since it was used by Julius Caesar adoptive son and successor, emperor Augustus, to reinforce its political power.

The visions of antique philosophers Aristotle (384-332 B.C) and Seneca (4 B.C. - 65 A.D) is also worth mentioning. Aristotle explanation to the comet phenomenon were quite exceptional, not because they were accurate, but because they were physical in nature and devoid of superstitious or astrological ideas (Yeomans 1991). In his treaty *Meteoritica*, he explained that the comets are an atmospheric phenomenon consisting in 'dry and warm exhalations' ignited by friction below the heavens. The shape of the comet would be the result of the exhalation properties, and their frequency could predict droughts and winds because they were formed in those conditions. As most Greek philosophers (with the notable exception of Pythagoras), Aristotle did not consider comets as astronomical objects but rather atmospheric phenomenons.

Roman politician and philosopher Seneca had a more modern view and considered comets as celestial objects with their own orbits, travelling in a uniform manner, and that could not be seen when beyond the planets. In his *Natural Questions*, Seneca interestingly reflects on the limit of his own knowledge and the scientific process by which the mysteries of comets will be unveiled more than a millennium later (Yeomans 1991; Eicher 2013):

> *The day will yet come when posterity will be amazed that we remained ignorant of things that will do them seem so plain... Men will some day be able to demonstrate in what regions comets have their paths, why their course is so far moved from the other stars, what is their size and constitution. Let us be satisfied with what we have discovered, and leave a little truth for our descendants to find out.*
>
> *... it is essential that we have a record of all the appearances of comets in former times. For, on account of their infrequency, their orbit cannot as yet be discovered or examined in detail, to see whether they observe periodic laws, and whether some fixed order causes their reappearance at the appointed day.*

It was unfortunately Ptolemy's view and superstition that dominated the work of astronomers for the centuries to come through the Middle Ages. Comets have been associated with historical and often disastrous event, like the outbreak of the terrible Justinian plague in 541 A.D., the fall of Genghis Khan empire, or the Istanbul earthquake of 1556 (Figure 1), to name a few.

2.1.2 The Scientific Renaissance

Understanding of comets true nature and orbit came with more precise instrumentation and the development of the scientific method during the Renaissance. Precise observations by

Figure 1: Colored woodcut Depicting damage in Istanbul from the May 10, 1556, earthquake, with the 1556 comet taking an important place in the image. Printed by Herman Gall in Nuremberg, 1556. Image source: wikimedia commons

Tycho Brahe of the Comet C/1577 V1 (Brahe 1578) allowed him to demonstrate that the parallax of the comet was less than 15 arcminutes, placing it at a distance greater than the Moon. Before Brahe's work, comets were still commonly considered as atmospheric events. During the following decades, efforts were made by astronomers to calculate the orbit of comets. Dörfell, observing C/1680 V1 in 1680 and 1681, found that it was the same comet before and after perihelion, explaining why comets were usually seen in pairs for the first time (Festou, Keller, and Weaver 2004). With his *Philosophiae Naturalis Principia Mathematica* (Newton 1687), Newton postulated its law of gravity that would be primordial in understanding comet orbits and origins. It was Halley, Newton's editor, that computing cometary orbits with Newton's law of gravity and comparing its results to historical data discovered the periodical nature of comets. He predicted the return of the Great Comet

of 1682 in 1758 (Halley 1705). He did not live to see the return of the comet, but the prediction was confirmed and the probably most observed comet in History now bears his name, 1P/Halley.

Halley's discovery was a milestone in cometary science, an important step leading to the current scientific understanding of comets. Other discoveries and the modern viewpoint on comets are discussed in the rest of this section.

2.2 The dynamical classification and origin of comets

Comets formed from the aggregation of icy grains in the solar nebula (Paul R Weissman, Asphaug, and Lowry 2004), during the birth of the solar system 4.65 billion years ago. They formed at a large distance from the Sun in the region of the giant planets, allowing the incorporation of volatiles in the form of ices. During the evolution of the solar system, comets have been scattered by the influence of the giant planets into new reservoirs (Morbidelli and H. Levison 2003).

Following the work of other astronomers from the first half of the 20th century, Jan Oort hypothesised in 1950 from a dynamical study of the semi-major axis of observed comets, that long period comets come from a region between about 50 000 and 150 000 AU (Oort 1950). He postulated the existence in this region of a cloud containing about 10^{11} observable comets; the exact number of comets in this cloud is still a subject of debate today. The range of eccentricities of long period comets indicated that the cloud must be isotropic. This reservoir of comets in the outer part of the solar system has been called the 'Oort cloud' (Figure 2). Comets can be expelled from the cloud, possibly towards the inner part of the solar system, due to the interaction with other stars or galactic tides. Those visiting the inner solar system are most likely 'new' comets, coming close to the Sun from the first time since their formation.

Edgeworth 1949 and Kuiper 1951 argued for the existence of another reservoir of icy bodies, that would extend outside the region of giant planets in the ecliptic plane (Figure 2). Those objects could be the source of a population of comets with low eccentricity. The trans-Neptunian objects in this region are actually divided into two main groups (Opitom 2016), the Kuiper Belt and the Scattered Disk. The Kuiper Belt extends above the orbit of Neptune, from 30 to 50 AU. Its population is dynamically stable and does not cross the orbit of Neptune. The Scattered Disk contains a more eccentric population whose orbit is unstable over the long term because of the influence of Neptune. Its population has a semi-major axis larger than 50 AU and a perihelion close to Neptune. Unlike Oort cloud objects, some Kuiper Belt objects have been directly observed (Jewitt and Luu 1993) and one Kuiper Belt

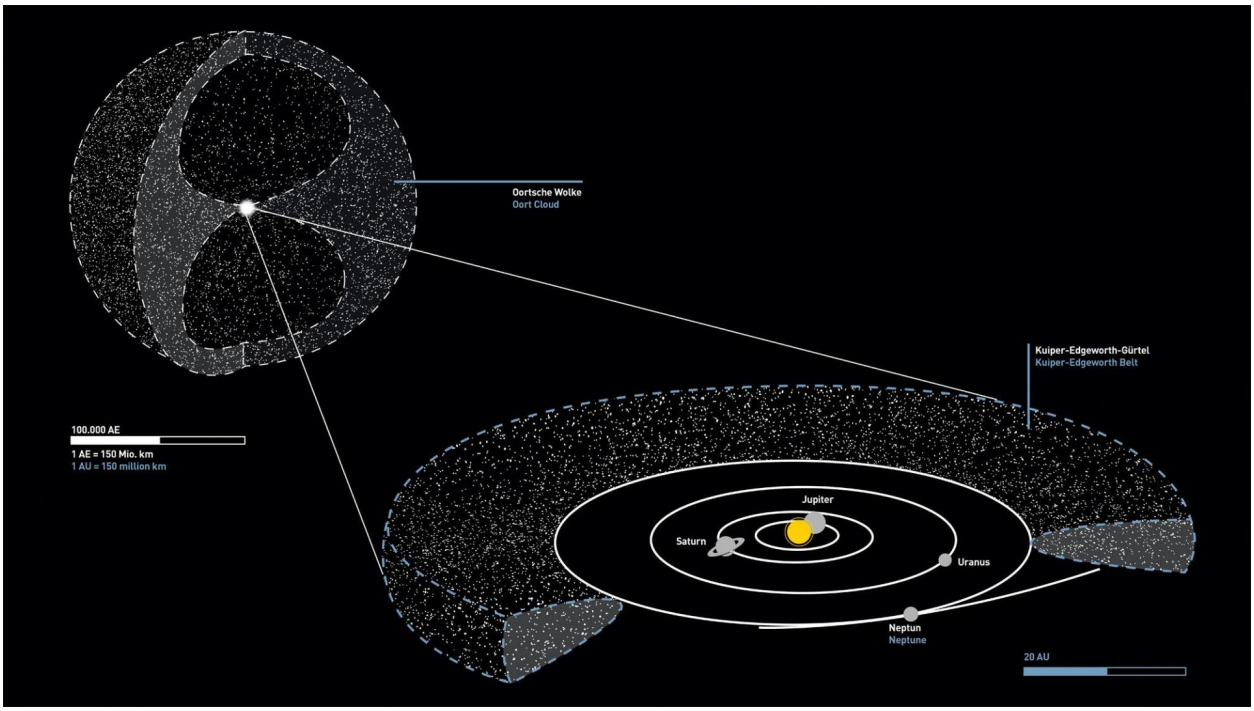

Figure 2: The two main comet reservoirs in the solar system. The Kuiper belt (bottom right), extending from 30 to 50 AU from the Sun in the ecliptic plane, and the Oort cloud (top left), extending radially up to 100 000 AU from the Sun. Credit: Daniel Röttele, DLR (dlr.de)

object, Ultima Thule, was even flyby by the New Horizon probe (Stern et al. 2019).

In recent years, a new class of active objects has been discovered in the main asteroid belt between Mars and Jupiter, which may be another reservoir of comets in the solar system. Main-belt comets have the orbital properties of asteroids but the physical properties of comets (Jewitt 2012). They should not be confused with active asteroids whose activity is more varied. While the activity of comets originates exclusively from the sublimation of ices, activity of active asteroids has been found to be the result of sublimation, impacts, or is still unclear. Hypothesis on what drives the activity of active asteroids can be found in Jewitt 2012.

With the goal to create a coherent classification of comets, Levison 1996 developed a system based on a three body problem Sun-Jupiter-comet (Figure 3). The classification is based on the Tisserand parameter (with respect to Jupiter):

$$T_J = \frac{a_J}{a} + 2cos(i)\sqrt{\frac{a}{a_J}(1-e^2)} \tag{1}$$

where a_J is Jupiter's semi-major axis and a, e and i are the comet semi-major axis, ec-

centricity and inclination, respectively. Comets with $T_J < 2$ are called 'nearly isotropic' because they have a fairly uniform inclination distribution. They most likely originates from the Oort cloud. They are divided in new and returning comets depending on the size of the semi-major axis of their orbit. Comets with $T_J > 2$ are called 'ecliptic' because they have a mostly flat inclination distribution. Ecliptic comets are further divided depending on whether they lie inside Jupiter's orbit (Encke type), outside Jupiter's orbit (Chiron type), or crossing Jupiter's orbit (Jupiter family comets). Levison 1996 argues that almost all comets stays in one of these classes throughout their entire lifetime, making this classification robust and dynamically significant.

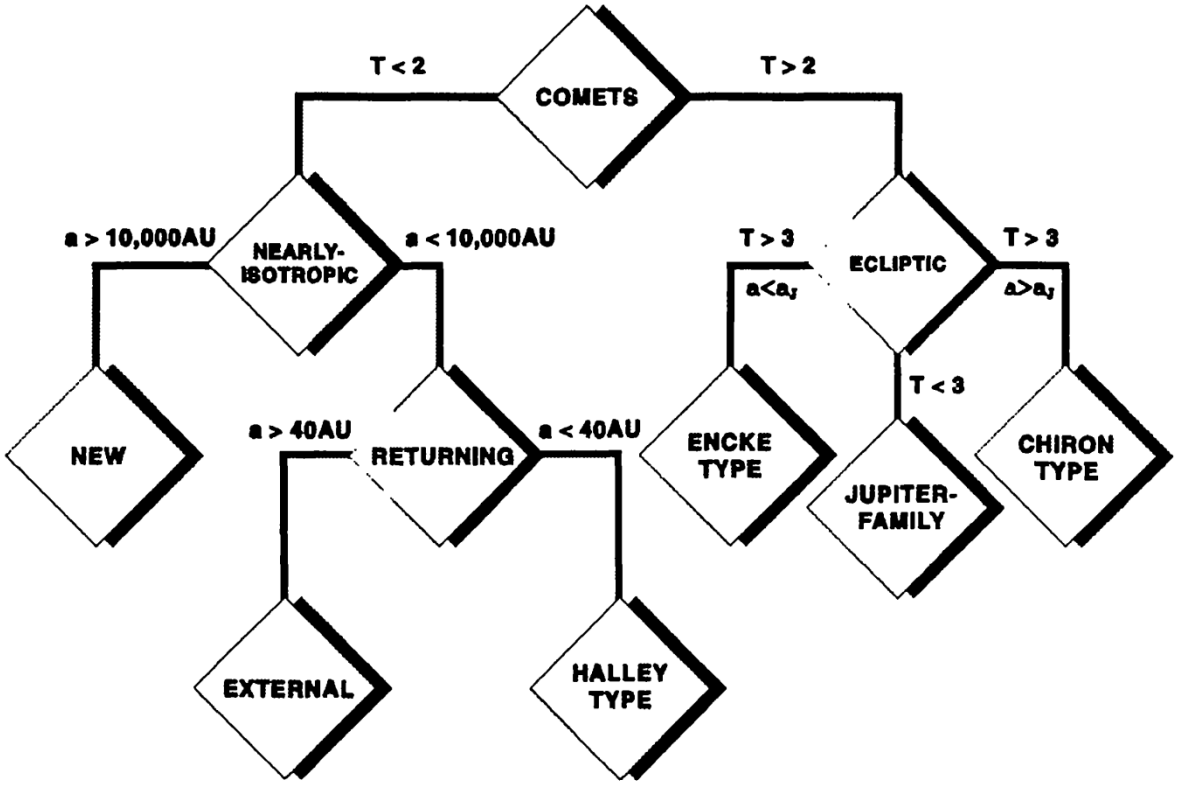

Figure 3: Comet dynamical classification according to Levison 1996

2.3 The physical properties of comets

2.3.1 The nucleus

The nucleus of a comet is very difficult to observe from the Earth. When the comet is far away from the Sun, it is inactive and too faint to be observed. If its orbit brings it close enough to the inner solar system, sublimation of the ices form the coma that outshines the nucleus, effectively hiding it. Some information can still be collected from afar, with unresolved

observations, as the color or the albedo of the nucleus, but more precise studies of the properties of the nucleus require space missions. The most recent was the Rosetta mission from the European Space Agency to comet 67P/Churyumov-Gerasimenko (Figure 4). From such space missions, we know that comets are made of half ice and half refractory material. Ices are composed of 80% of H_2O, 10 to 20% of CO_2 and CO, and tens of minor components, comprising complex organic molecules (Opitom 2016).

The inner structure of comets is still poorly known. Whipple 1950 famous 'dirty snowball' model views comets as an monolithic conglomerate of ice and rocky materials. This model was the first to be able to explain outgassing and non-gravitational motion of comets. The 'primordial rubble pile' model was later proposed as a modification of the Whipple model, after spacecraft observations suggested that comet were not consolidated single bodies (Paul R. Weissman 1986). In the rubble pile model, the nucleus is composed of weakly bounded agglomerations of smaller fragments. This model is supported by events showing the structural weakness of comets, as the shedding of fragments and tidal disruption of Shoemaker-Levy 9 during its encounter with Jupiter (Asphaug and Benz 1996). These properties are supporting the formation scenario of comets of accretion in the solar nebula (Paul R Weissman, Asphaug, and Lowry 2004).

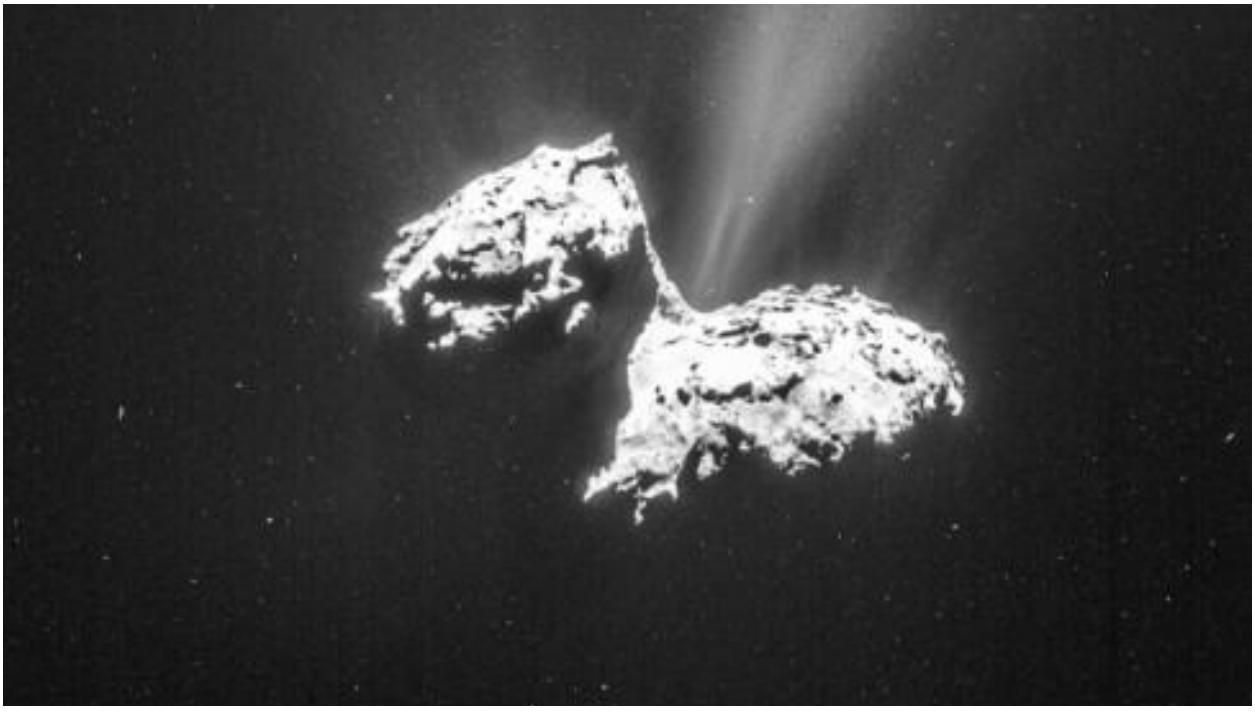

Figure 4: Comet 67P/Churyumov-Gerasimenko photographed by the Rosetta navigation camera (NAVCAM) on 6 February 2015 at 124.0 km from the nucleus. Source: ESA/Rosetta/NAVCAM.

2.3.2 The coma

The coma is a cloud of gas and dust surrounding the comet, formed by the sublimation of the nucleus surface ice. As the gas molecules escape the nucleus, they carry over the dust in the process at high speeds of about 1 km/s and 200 m/s for the gas and dust, respectively, for a comet at 1 AU from the Sun (Moulane 2021). Cometary activity is strongly dependant on the distance to the Sun, because of the amount of solar radiation received, but also because ices of different compositions will have different sublimation temperatures. At distances within 3 AU from the Sun, sublimation of H_2O ice is the main driver of cometary activity, while CO and CO_2 ices sublimation are relatively more important than H_2O at higher distances. The size of the coma depends on the distance to the Sun and the specie observed, but it can reach hundreds of thousands of kilometres at 1 AU from the Sun (Opitom 2016).

Species directly released from the ice into the coma are named parent (or primary) species (Figure 5). Different chemical and physical processes can lead to the destruction of those species into daughter (or secondary) species. The main process by which parent species are destroyed is photodissociation. Daughter species can continue to react, enhancing the

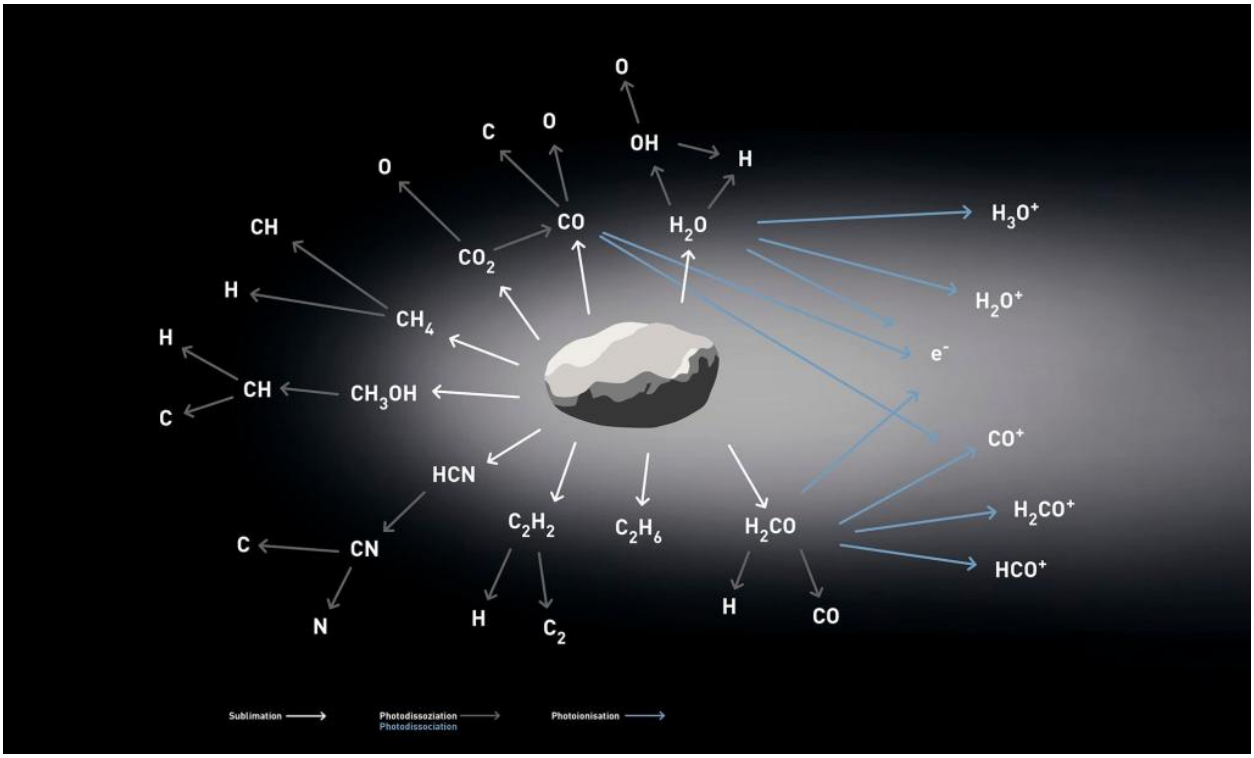

Figure 5: Parents and daughter molecules, along with some processes regulating the chemistry of the coma. Sublimation of ice volatiles (white arrows) releases parent species into the coma. Photochemistry driven by the Sun leads to photodissociation (grey arrows) and photoionization (blue arrows) of parent species. Credit: DLR (dlr.de)

chemistry of the coma. An overview of the type of reactions that can occur in the coma is presented in Table 1.

Photodissociation	$h\nu + H_2O \longrightarrow H + OH$
Photoionization	$h\nu + CO \longrightarrow CO^+ + e$
Photodissociative ionization	$h\nu + CO2 \longrightarrow O + CO^+ + e$
Electron impact dissociation	$e + N_2 \longrightarrow N + N + e$
Electron impact ionization	$e + CO \longrightarrow CO^+ + e + e$
Electron impact dissociative ionization	$e + CO_2 \longrightarrow O + CO^+ + e + e$
Positive ion-atom interchange	$CO^+ + H_2O \longrightarrow HCO^+ + OH$
Positive ion charge transfer	$CO^+ + H_2O \longrightarrow H_2O^+ + CO$
Electron dissociative recombination	$C_2H^+ + e \longrightarrow C_2 + H$
Three-body positive ion-neutral association	$C_2H_2^+ + H_2 + M \longrightarrow C_2H_4^+ + M$
Neutral rearrangement	$N + CH \longrightarrow CN + H$
Three-body neutral recombination	$C_2H_2 + H + M \longrightarrow C_2H_3 + M$
Radiative electronic state deexcitation	$O(^1D) \longrightarrow O(^3P) + h\nu$
Radiative recombination	$e + H^+ \longrightarrow H + h\nu$
Radiation stabilized positive ion-neutral association	$C^+ + H \longrightarrow CH^+ + h\nu$
Radiation stabilized neutral recombination	$C+C \longrightarrow C2+h\nu$
Neutral-neutral associative ionization	$CH + O \longrightarrow HCO^+ + e$
Neutral impact electronic state quenching	$O(^1D) + CO_2 \longrightarrow O(^3P) + C$
Electron impact electronic state excitation	$CO(^1\Sigma) + e \longrightarrow CO(^1\Pi) + e$

Table 1: Overview of the different reactions types taking place in the coma by order of importance, with examples. From Newburn, Neugebauer, and Rahe 1991

2.3.3 The tail

The most photogenic features of a comet are probably its tails (Figure 6), that can span over several tens of millions of kilometres (Opitom 2016). Interaction between the solar wind and the coma produces the ion (also called plasma) tail. Ions, mainly CO^+, gives it its blue color. It is straight and directed radially away from the Sun, following the direction of the solar wind. The dust tail is composed of dust particles pushed away by the radiation pressure. It has a white color because of the scattering of the sunlight. A third, neutral tail of sodium has been observed in comet Hale-Bopp, but its origin is still unclear (Cremonese et al. 1997).

Figure 6: Comet Neowise on July 19, 2020. The blue ion tail is pointing directly away from the Sun. The white dust tail is pushed away by radiation pressure. Credit: Zixuan Lin.

2.4 Comets: a conceivable answer to fundamental questions

2.4.1 Fossils of our solar system

Comets are considered as fossils of the solar system. They formed at the same time as the solar system, 4.6 billion years ago, from agglomeration of ice grains of the solar nebulae, and possibly from surviving interstellar grains (Weidenschilling 2004). Since their reservoir is in the cold region of the outer solar system, they did not alter and kept the composition of the solar nebulae where they formed, providing a cosmogenic record of the composition of our protoplanetary disk and the conditions within it. Their chemistry may have been altered if they travelled close to the Sun during their lifetime, or by galactic cosmic rays, but those alterations would only affect a thin layer near the surface.

Comets are therefore important in constraining the models of the evolution of the solar system. For example, with a recent developed model for the evolution of the solar system, the

Nice model (Tsiganis et al. 2005; Gomes et al. 2005). The Nice model explains the different dynamical populations of the Kuiper Belt by the migration of giant planets. According to the model, icy bodies formed a dense population in the protodisk. They formed in the region of the giant planets between 10 and 15 AU, closer to the Sun than the actual Kuiper Belt. The migration of giant planets, when the solar system was about 500 millions years old, scattered the inner part of this disk and sent icy bodies on orbits further away, with different kinds of inclinations and eccentricities (Figure 7, Morbidelli and H. Levison 2003). This resulted in what we observe today in the Kuiper Belt: (a) a (dynamically) cold population in the ecliptic with low inclination and eccentricity, presumably objects that were less affected by the migration of giant planets and formed where they are now and (b) a (dynamically) hot population with a higher eccentricity and inclination, the population that was presumably scattered and originated from an inner region of the solar system. The further away Oort cloud would be composed of icy bodies that actually formed in the region of the gas giants, closer to the Sun than the cold population of the Kuiper Belt. Hot and cold populations are a dynamical classification, but the study of the color of those objects showed that the composition of the hot and cold population are also statistically different. An extensive survey of the chemical composition of those objects would further constrain models.

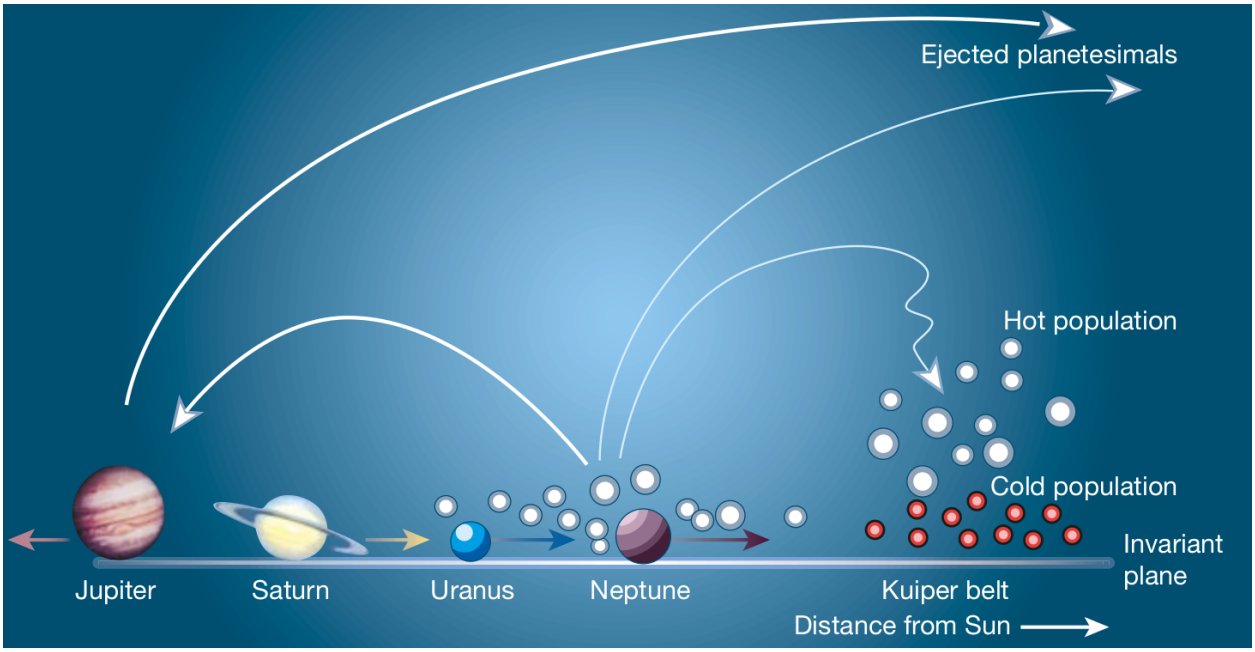

Figure 7: Ejection of the small bodies formed within the orbit of Neptune by the migration of giant planets. The cold population (in red) is less affected by the migration, while the hot population (in white) migrates from the giant planet region towards the outer part of the solar system. From Morbidelli and H. Levison 2003.

2.4.2 Prebiotic chemistry

How life appeared on Earth is a very hot topic, and still poorly understood. The late-veneer hypothesis suggests that an important amount of material, including water and organics, were brought to the Earth after its initial accretion, around 4 billion years ago (Anders 1989), and before the apparition of life around 3.46 billion years ago (Ueno et al. 2006). It is possible that those organics coming from space were, at least partially, at the origin of the development of life on Earth. Amino-acids are interesting molecules to look for, since they are the building blocks of proteins, macromolecules serving as the functional molecule of life by accomplishing many functions in all living organisms.

Comets are possible late-veneers and could have brought amino-acids to the Earth, therefore tentatives were made to detect them on comets. Two notable detection were made by space missions. NASA Stardust was a sample return mission launched in 1999, targeting the comet Wild2. The comet surrounding gas and dust was captured in aerogel cells during the spacecraft flyby in the coma and the sample was successfully returned to Earth in 2006. Laboratory analysis revealed the presence of at least 11 different amino-acids (Glavin, Dworkin, and Sandford 2008) but only glycine was present at a different concentration than witness samples and had different isotopic composition compared to terrestrial amino acids (Elsila, Glavin, and Dworkin 2009). It has been established that the detected glycine is from extraterrestrial origin, but uncertainties remain about its presence in the comet, since collected molecules could possibility be chemically modified during impact with the gel (Sandford 2008), or the extraction of the sample from precursors such as HCN (Glavin, Dworkin, and Sandford 2008).

More recently, the mass spectrometer onboard the ESA Rosetta spacecraft, launched in 2004, found unambiguous evidences of glycine in the atmosphere of comet 67P/ Churyumov-Gerasimenko (Altwegg et al. 2016). The detection of glycine was made multiple times at perihelion, and contrarily to the Stardust sample, did not suffer from chemical preparation of the sample or contamination.

2.4.3 Water on Earth

Earth formation models indicate that the Earth should have lost its primordial water at an early age from evaporation. There is no consensus on the origin of today Earth water. Comets are an important reservoir of water ice in the solar system and could have contributed to filling Earth's oceans during the late-veneer bombardment, even partially.

The deuterium/hydrogen (D/H) ratio in an icy body is related to the distance from the Sun at which it formed, and can be used to determine if two bodies originates in similar

chemical and physical conditions. In the warmer regions of the protodisk, icy planetisimals can sublimate and exchange hydrogen and deuterium atoms in the gas phase (Ceccarelli et al. 2014). For kinetic reasons, this mechanism will reduce the deuterium increasingly the closer to the Sun. Since this fractionation process does not happen in the solid phase, the observed deuterium ratio should be representative of the local values where the ice on the object condensed. Also, gas-grain reactions could be responsible for deuterium enrichment in the cold outer part of the solar nebulae. Whatever the mechanism, those models are consistent with a deuterium enrichment from low values close to the Sun to high values in the outer part of the disk.

Figure 8 shows the D/H ratio measured from different comets, the Earth oceans (D/H $= 1.5 \times 10^{-4}$), and other bodies of the solar system. Sampled Oort cloud comets have generally a higher value of D/H ratio than the Earth oceans, and are unlikely the source of the Earth's water. The two Jupiter family comets 45P and 103P (observed with the Herschel Space Telescope) have D/H ratios similar to the Earth's one. However, 67P (D/H $= (5.3 \pm 0.7) \times 10^{-4}$, measured by *in situ* mass spectroscopy), another JFC, is not consistent with the rest of this group showing a D/H ratio more than 3 times higher. An explanation to this discrepancy could be that there are chemically different subgroups in the JFC, another

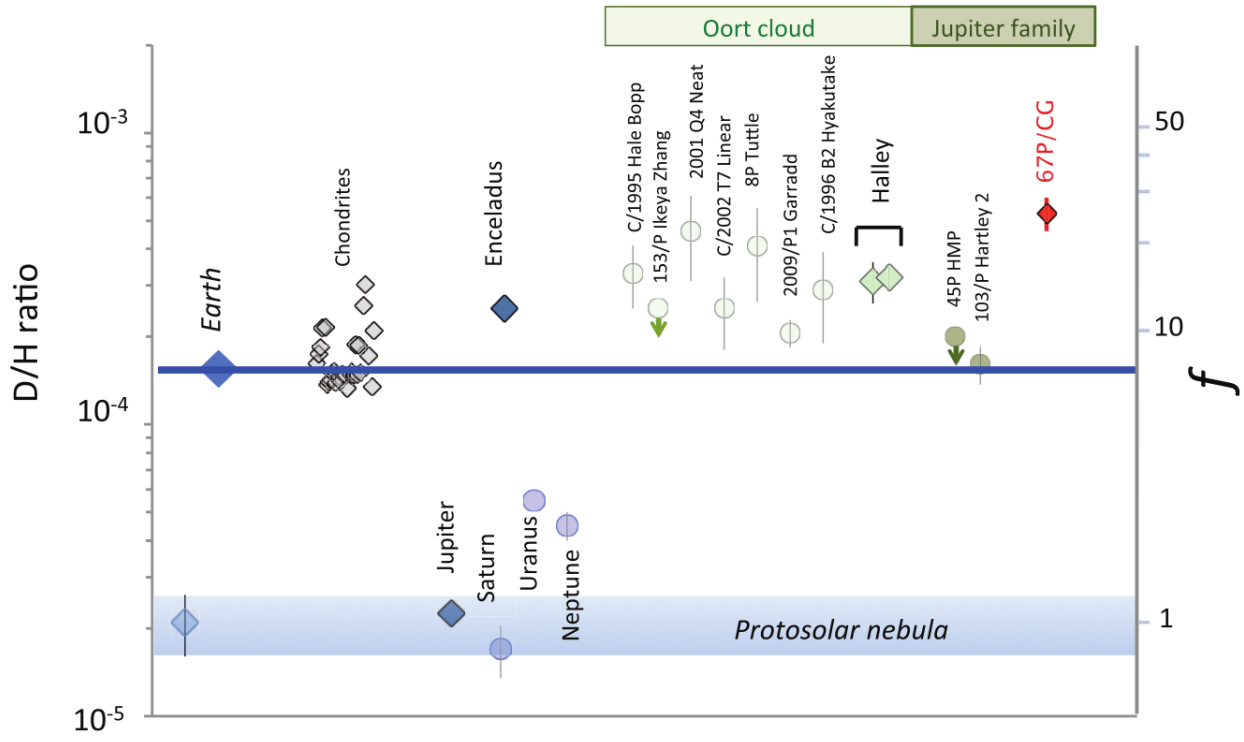

Figure 8: D/H ratio of different comets, the Earth's oceans, and other bodies of the solar system. From K. Altwegg et al. 2015.

is the accuracy of the Hershell measurements and modelisation needed to retrieve D/H ratio from spectroscopic data. Those observations, except maybe for a sub-population of the JFC, do not support the hypothesis of the cometary origin of Earth's water. Chondrites D/H ratio, on the other hand, are similar to the Earth's, making them more interesting candidates. However, very few comets (especially JFC) have been sampled so far, and not necessarily accurately. Future instruments like ELT/METIS will be more appropriate to accurately sample the D/H ratio of comets.

2.5 On the necessity of a multi-wavelength approach to the study of comets

Not all molecules in the coma are observable in the same region of the electromagnetic spectrum. Parents species (see Figure 5), coming from the direct sublimation the nucleus ices (as H_2O, CO, CO_2, H_2CO, CH_3OH, CH_4, C_2H_2, C_2H_6, HCN, NH_3), and their isotopes are mainly observable in the infrared (IR) domain. Daughter species, products of the photochemistry of parent species induced by the Sun (as OH, NH, CN, CH, C_2, C_3, and NH_2), are observable mainly in the ultra-violet and visible (UV-Vis) regions of the electromagnetic spectrum. Daughter species abundances do not necessarily reflect the composition of the nucleus. Indeed, different physical and chemical processes are involved in the formation of daughter species (see Table 1). Therefore, an accurate modelling to correlate them to parent molecules is needed. Probable parent molecules for some observed species in comets are given in Table 2. In addition, under the right conditions, parent molecules can be released from the dust grains (namely extended sources, Quirico et al. 2016), complexifying the chemistry of the coma.

Understanding the chemistry of the coma (and its connection to the chemistry of the nucleus) is also necessary to create a chemical taxonomy of comets. Indeed, there is an undergoing effort in the community to create a chemical taxonomy of comets, and possibly linking it to their dynamical distribution. The task is difficult since with limited observation possibilities, comets spending a fair amount of lifetime in the outer part of the solar system where they are not observable, it is difficult to make a statistically significant sampling of the different dynamical populations. By regrouping UV-Vis observations from 85 comets, A'Hearn et al. 1995 found two distinct chemical classes, 'typical' and 'carbon depleted' comets, based on their C_2 and C_3 abundances (A'Hearn et al. 1995; D. Bockelée-Morvan and Biver 2017). They also found that the fraction of carbon depleted comets is statistically more important in Jupiter family comets than in Oort cloud comets. This trend was later confirmed by Cochran, Barker, and Gray 2012 over a sample of 130 comets, while a more

Observed species	Possible parent molecules
H_2O,H_2O^+,OH,H	H_2O
CO_2^+	CO_2
CO,CO^+,C	CO,CO_2
CH	CH_4
CN	HCN,C_2N_2
NH_2	NH_3
NH	NH_2,NH_3
C_2	C_2H_2,C_3H_2O
C_3	C_3H_4,C_3H_8
CS	CS_2,OCS
S	S_2,OCS,CS_2,H_2S,SO_2
O	O_2,CO_2,CO,H_2O

Table 2: Observed species and their possible parents molecules. From Swamy 2010

complex taxonomy also based on carbon, containing seven classes of comets was advanced by Scheicher and Bair 2014 from the observation of 107 samples. However, those first attempts are not enough to relate the chemical composition of comets to their evolutionary process or original population distribution. The too poorly understood parent/daughter species relation also complicates the effort of making a chemical classification of comets.

Even with increasing observations and understanding of comet spectra, the results obtained in the UV-Vis and IR are not always in agreement. A common chemical classification of comets does not exist, and the links between parent, daughter and extended species observed in the coma are poorly portrayed. Those fields of investigation could strongly benefit from a coordinated effort between experts of both the UV-Vis and the IR (and eventually the microwave domain) with the logistical capabilities to make simultaneous high resolution spectroscopy observations in both domains. In the history of high resolution spectroscopy of comets, there had been only few attempts to jointly observe the same target at multiple wavelength regimes (e.g. Jehin et al. 2009). Although reports on observations of a same comet at different wavelength are not uncommon, they are made by different non-collaborating teams with different data processing approach and not necessarily during the same night, making it more difficult to study the relation between parent and daughter species.

3 Infrared spectroscopy

Spectroscopy is the study of electromagnetic waves and matter interaction by the absorption or emission of a photon. Such interactions are associated with a change of excitation state of a molecule, with the difference of energy between the old and new state corresponding exactly to the photon energy. Since the energy of the different excitation states, ruled by quantum physics, is dependent on the molecule composition and structure, spectroscopy is a common and powerful method to derive the chemical composition of a comet (or any other celestial bodies), even at a great distance.

Spectroscopic features in the UV-visible region of the spectrum are associated with changes in the electronic state of a molecule (possibly with changes in vibrational and rotational states), in the infrared (IR) region with changes in its vibrational state (possibly with changes in rotational state), and in the microwave region with changes in its rotational state.

The following section is focused on the principle behind infrared (∼1000 to 0.77 µm) spectroscopy and how it relates to identify and possibly quantify parent molecules in the comet's coma. A more throughout demonstration of the relations resulting from quantum mechanic presented hereafter can be found in textbook (used here are McQuarrie 2008; Hollas 2004; Banwell 1983).

3.1 The infrared spectrum of a diatomic molecule

One simplistic way to describe vibrations in a diatomic molecule is to consider a harmonic oscillator, a system consisting of two particles of masses m_1 and m_2 (the atoms) connected by a spring (the chemical bond) of constant force k (Figure 9b). The system is free to vibrate and does so with a vibration frequency ω_{osc}, given by Hook's law:

$$\omega_{osc} = \frac{1}{2\pi}\sqrt{\frac{k}{\mu}} \tag{2}$$

where $\mu = (1/m_1 + 1/m_2)^{-1}$ is the reduced mass of the system. Solving the Shrödinger equation for the Hook's law, it is possible to find the vibrational energies associated with this system:

$$E_v = (v + \frac{1}{2})h\omega_{osc} \tag{3}$$

with h the Planck constant and v the vibrational quantum number. v can only take positive or zero integer values ($v = 0, 1, 2, ...$), resulting in E_v having discrete values. From Equation 3 we can see that in the case of the harmonic quantum oscillator, E_v is dependent on the

vibration frequency ω_{osc} and therefore the particle masses and the bond strength. In addition, energy levels are equally spaced by $h\omega_{osc}$ and $E_0 = \frac{1}{2}h\omega_{osc} \neq 0$, as can be seen in Figure 9c. It also results from the Shrödinger equation that for a vibrational transition to happen, the dipole moment of the molecule needs to change during the normal mode motion, to interact with the electric field of the electromagnetic radiation, and the following selection rule must be respected:

$$\Delta v = \pm 1 \tag{4}$$

Those concepts can be expanded to polyatomic molecules with more than two atoms. The number of normal vibrational modes is $3N - 5$ for linear molecules and $3N - 6$ for non-linear molecules, with N the number of atoms (Figure 9c).

Molecules, however, do not behave perfectly as harmonic oscillators. For instance, the parabolic nature of the harmonic potential does not reflect that atoms stop interacting at high internuclear distance (when the chemical or physical bound is broken). In the anharmonic approximation, the bound is described by the Morse function instead of the Hook's law. Solving the Shrödinger equation for the Morse function gives a power series (whose only the

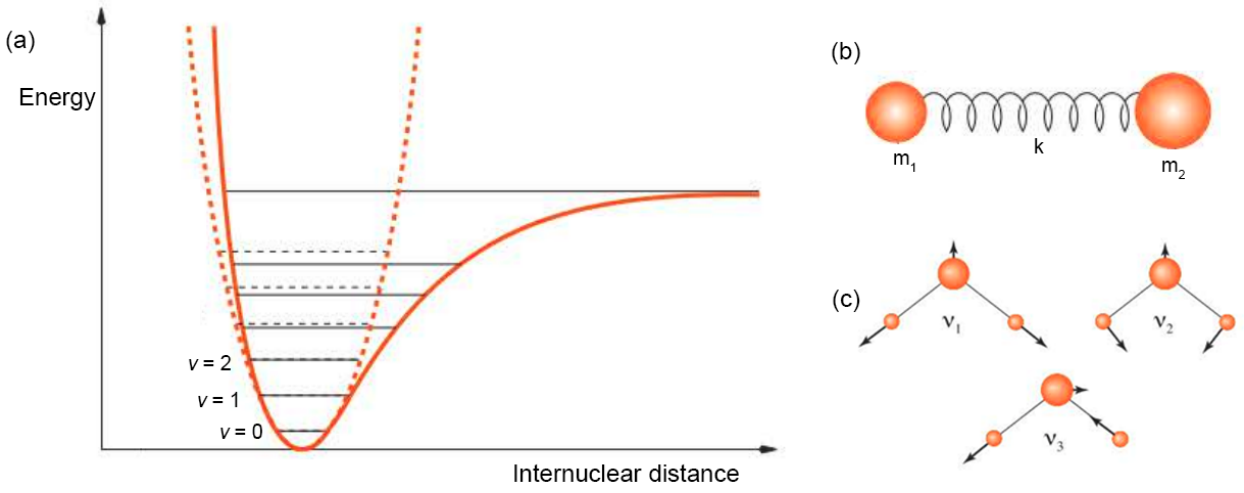

Figure 9: The diatomic oscillator. (a) Potential energy for a harmonic oscillator (dashed line) and an anharmonic oscillator (plain line). The energy levels for different vibrational numbers are shown in black. The potential energies in the harmonic and anharmonic cases are equivalent at low values of v, but differ for higher values of v. (b) Representation of the two masses connected by a spring model for a diatomic molecule. (c) Normal vibrational modes of water: symmetric stretching (υ_1), symmetric bending (υ_2), and antisymmetric stretching (υ_3). The 3 modes are accompanied by a change in the electric dipole of the molecule and are infrared active. Adapted from McQuarrie 2008.

2 first terms are considered here):

$$E_v = (v + \frac{1}{2})h\omega_e - (v + \frac{1}{2})^2 h\omega_e x_e + ... \tag{5}$$

where ω_e is the anharmonic oscillation frequency and x_e the anharmonicity constant. The first term of Equation 5 is similar to the harmonic oscillator energy (Equation 3). The second term is responsible for the decrease of spacing between the energy levels as v increases, since x_e is a positive number much smaller than 1. The overall shape of the Morse potential is represented in Figure 9a. If the molecule is in its ground state (a good approximation at low temperature), the harmonic and anharmonic approximations are close.

In reality, vibrational transitions are accompanied by rotational transitions and one needs to consider the rotational energy states while analysing the infrared spectrum of a molecule. The rotational transitions of a diatomic molecule can be approximated, independently of the vibrational motion, by considering a diatomic molecule as a rigid rotator (Figure 10a). The moment of inertia I of the rigid rotator with respect to its rotation axis is given by

$$I_B = \mu l^2 \tag{6}$$

with μ the center of mass of the rigid rotator and l the distance between the 2 particles. From the Shrödinger equation it is possible to find that the energy of the system is given by

$$E_J = \frac{h^2}{8\pi^2 I_B} J(J+1) \tag{7}$$

where J is the rotational quantum number. J can only take positive or zero integer values ($J = 0, 1, 2, ...$), resulting in E_J having discrete values. For simplicity we can define the rotational constant B as

$$B = \frac{h^2}{8\pi^2 I_B} \tag{8}$$

The difference between two rotational energy levels is given by

$$E_{J+1} - E_J = B(2J+2) \tag{9}$$

which means that the difference between rotational energy levels increases by $2B$ for each increase of J (Figure 10b) and upper energy levels are more spaced than lower ones. For a rotational transition to take place, the molecule needs to own a permanent dipole and the transition must satisfy the selection rule

$$\Delta J = \pm 1 \tag{10}$$

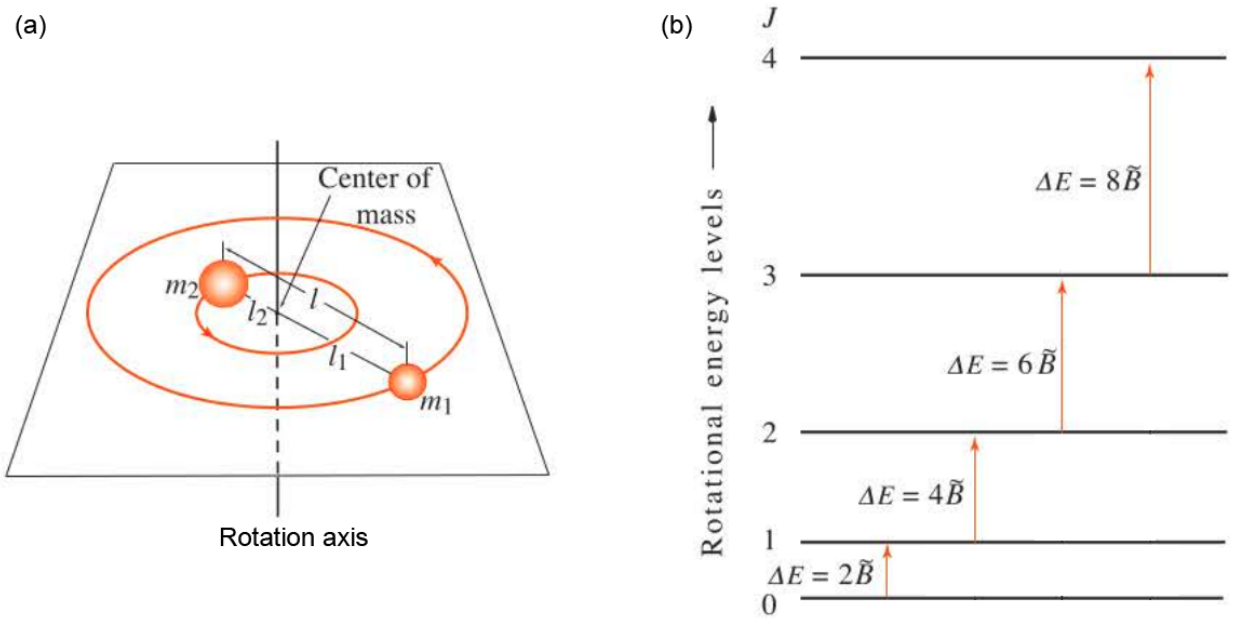

Figure 10: The diatomic rigid rotator. (a) Representation of the diatomic rigid rotator model. (b) Rotational energy levels of a rigid rotator. Adapted from McQuarrie 2008.

Molecules do not exactly act as rigid rotator, however, due to the centrifugal force stretching the bond during rotation. A corrective term can be added to Equation 7 for a non-rigid rotator:

$$E_J = BJ(J+1) - DJ^2(J+1)^2 \tag{11}$$

with D the centrifugal distortion constant, a positive number. As for the anharmonicity correction of the harmonic oscillator approximation, the correction for a non-rigid rotator results in the decrease of energy of rotational levels with greater the correction the higher J.

If we consider that rotation and vibration are independent of each other, we can combine the vibrational and rotational motions for a diatomic molecule in a rigid rotator-harmonic oscillator model by adding the contribution of the two motions. By adding Equation 3 and Equation 7, we get the ro-vibrational energy $E_{v,J}$:

$$E_{v,J} = (v + \frac{1}{2})h\omega_{osc} + BJ(J+1) \tag{12}$$

that contains the vibrational quantum number v and the rotational quantum number J. Different rotational states J are possible for a given vibrational state v (Figure 11a). Transitions need to respect selection rules for both the harmonic oscillator and the rigid rotator

approximations:

$$\Delta v = \pm 1 \qquad \text{and} \qquad \Delta J = \pm 1 \tag{13}$$

As a result, in the spectrum region corresponding to the $v = 0 \rightarrow v = 1$ transition, not one emission line is observed in the emission spectrum but an ensemble of emission lines each corresponding to a change of J (Figure 11b). The series of lines at higher frequencies than the band center (whose frequency is given by the pure vibrational transition from the fundamental state) is called the *R branch* and correspond to $J + 1$ transitions. The series of lines at lower frequencies than the band center is called the *P branch* and corresponds to $J-1$ transitions. The spacing between the line is constant and equal to $2B$ according to the rigid rotator model (see Equation 9) but it can be observed in Figure 11b that spacing between lines decreases slightly but constantly from the outer part of the P branch to the outer part of the R branch. The assumption that the vibration and oscillation can be considered separately (see Equation 12) is not exactly in line with reality. The increase of vibrational energy (an increase of v) comes with an increase of vibrational amplitude implying a more important mean interatomic distance l. Since B is inversely proportional to the square of l (see Equation 8 and Equation 6), the value of B decreases with v. This results in the reduction of the spacing between the lines of the R branch and increase of the spacing between the lines in the P branch with increasing J. The central Q branch (not indicated in Figure 11) corresponding to the pure vibrational transition ($\Delta v = +1$, $\Delta J = 0$) do not appear in the spectrum because it would violate the selection rule $\Delta J = \pm 1$. This is true

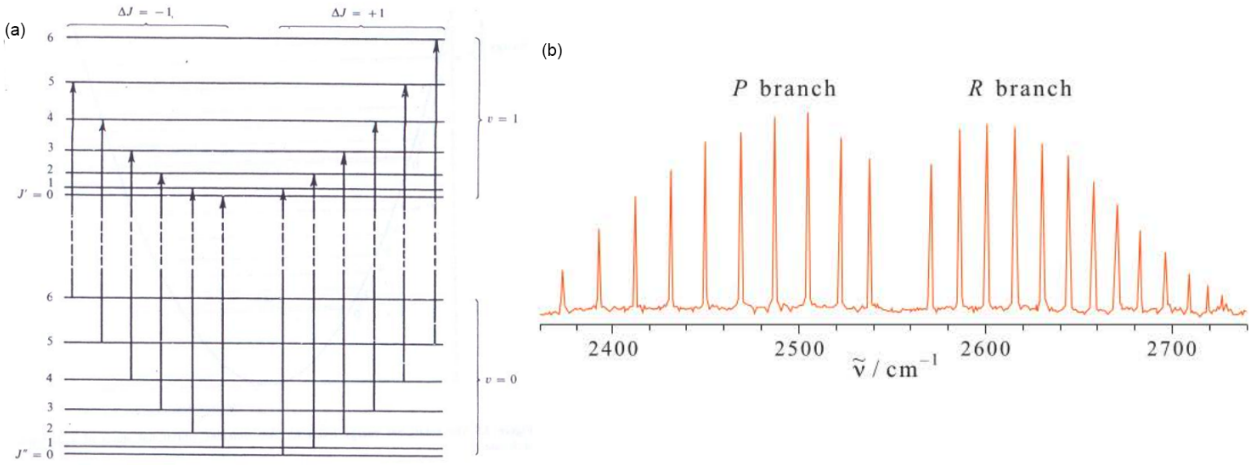

Figure 11: Energy levels and spectrum for a diatomic rigid rotator-harmonic oscillator. (a) Energy levels from $v = 0 \rightarrow v = 1$ with values of J up to 6. Each arrow represent transitions respecting the selection rules from $v = 0$. Adapted from Banwell 1983. (b) Ro-vibrational spectrum for the $v = 0 \rightarrow v = 1$ transition of $HBr_{(g)}$. Adapted from McQuarrie 2008.

for diatomic molecules, although the Q band can exist for other molecules as selection rules for a given transition depend on the symmetry of the system.

More complex molecules or specific cases will not be discussed here since the description of the interaction between infrared photons and molecules given above is sufficient to understand the extent of this work.

3.2 Infrared fluorescence of cometary volatiles

The 2 to 5 µm region is ideal to observe emission bands associated to ro-vibrational transitions of parent molecules in the cometary coma. This region receives abundant solar flux allowing for excitation of molecules, and reflection of the sunlight from the dust is not very strong (Lippi 2010). The main process leading to cometary emissions in the infrared is non-resonant fluorescence. This process consists, first, in the excitation of a molecule from its resting state into a high energy state by the absorption of a solar photon of the same energy as the difference between those two states. The molecule will spontaneously return to its resting state by releasing one or more photons of lower energy resulting from transitions to a lower energy state.

The main excitation process for most parent molecules is radiative excitation of the fundamental band of vibration by direct solar radiation (Bockelée-Morvan et al. 2004). For a ro-vibrational excitation $l \rightarrow u$ from a lower level l (characterized by quantum numbers J'' and v'', $v'' = 0$ for the fundamental band), to a upper level u (characterized by quantum numbers J' and v'), with $E_u > E_l$, the pumping rate (also called fluorescence efficiency) g_{lu} is given by

$$g_{lu} = \frac{c^3}{8\pi h \nu_{ul}^3} \frac{w_u}{w_l} A_{ul} J_{\nu_{ul}} \qquad [\mathrm{s}^{-1}] \tag{14}$$

with ν_{ul} the frequency of the transition, A_{ul} the Einstein coefficient for spontaneous emission of the transition $u \rightarrow l$ and w_u and w_l are the statistical weight of the upper and lower levels, respectively. $J_{\nu_{ul}}$ is the energy density of the solar radiation field at frequency ν_{ul}.

Other excitation mechanisms leading to fluorescence of the fundamental band of parent molecules are most of the time negligible. Electronic excitation could be accompanied by vibrational excitation and emissions visible in the infrared. However, excitation rates in the UV are lower than in the infrared due to the weaker flux of the Sun at those wavelengths. Furthermore, radiations in the UV leads to the photo-dissociation of parent molecules. In the microwave, excitation of pure rotational levels from the Sun radiation field is negligible due to the low flux of the Sun in that spectral region. However, excitation by the cosmic microwave background at 2.7 K can be important at distances > 3 AU from the Sun (Biver et al. 1999). Collisional excitation is not significant either for vibrational bands. Due to the

low temperature of the coma, the steady-state distribution of the vibrational population is determined by radiative processes described above. However, collisions with H_2O, or CO at large heliocentric distances, could be important in the inner part of the coma within a few kilometres of the nucleus surface. If collisions are frequent in that region, they could possibly maintain molecules in a higher excitation level and quench the fluorescence of vibrational bands.

For de-excitation, the flux emitted by the $u \rightarrow l$ ro-vibrational transition from an upper level u to a lower level l can be expressed as a function of the total molecular column density $\langle N \rangle$ by:

$$F_{ul} = \frac{\Omega}{4\pi} h\nu_{ul} g_{ul} \langle N \rangle \tag{15}$$

where Ω is the solid angle corresponding to the field of view and g_{ul} the emission rate for the $u \rightarrow l$ transition. This relation is valid for optically thin lines, which is a good approximation for most molecules thanks to the low density of the coma, but can break done close to the nucleus.

The measured molecular column can be used to estimate the relative molecular abundance in the cometary nucleus. To do so, it is necessary to calculate the production rates at the cometary nucleus from the measured molecular column. The most used model to do so is the Haser model (Haser 1957) that assumes a sublimation of the parent molecules at the surface of a spherical nucleus at a constant rate followed by a radial expansion at a constant speed. The relation between the production rate Q and the local density in the coma n for parent species in the Haser Model is then given by

$$n(r_c) = \frac{Q}{4\pi r_c^2 v_r} e^{-(r_c - r_n)/v_r \tau} \tag{16}$$

where r_c is the distance from the center of the nucleus, r_n is the radius of the nucleus, v_r is the radial outflow velocity and τ is the molecular lifetime of the parent specie. How $n(r_c)$ can be integrated to derive Q from $\langle N \rangle$ will depend on the measurement setup and instrument configuration (see Bockelée-Morvan et al. 2004 for a more complete review). v_r is a parameter that can also be derived from the spectrum, by analysing the radio line profile.

3.3 The Doppler effect

Comets have their own relative motion in the sky. The wavelength at which a given line is emitted is therefore shifted from the point of view of the observer by the relativistic Doppler

effect, depending on the comet relative velocity:

$$\lambda_{obs} = \lambda_s \sqrt{\frac{1 + v_c/c}{1 - v_c/c}} \tag{17}$$

where λ_{obs} is the observed wavelength, v_c is the line of sight velocity of the comet and c the speed of light in vacuum.

3.4 Telluric absorption

Absorption by molecules in the atmosphere leaves signatures in science target spectra taken from ground observatories. Telluric absorption is important in the infrared and can make the atmosphere partially or totally opaque at certain wavelengths (Figure 12). Atmospheric molecules having important absorption bands in the 1 to 5 µm region are H_2O, CH_4, CO_2, CO, N_2O, O_2, O_3 and OCS (MOLECFIT Pipeline team 2021; Smette et al. 2015), water vapour playing a crutial role for its considerable absorption bands in that region and the variability of its column density in the atmosphere. The effect of atmospheric absorption

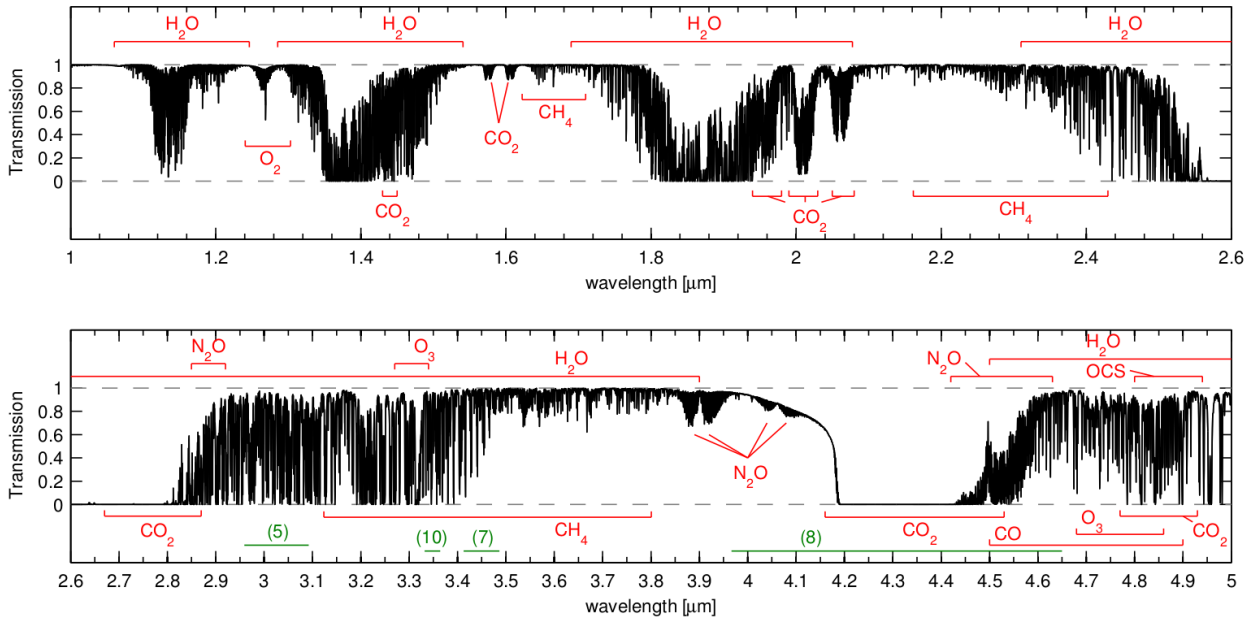

Figure 12: Atmospheric transmission from 1 to 5 µm computed with a resolution of $\lambda/\Delta\lambda = 10^4$. A transmittance of 1 indicates that the atmosphere is transparent at that wavelength, while a value of 0 indicates that all the radiation is absorbed by the atmosphere. The principal activity region of the eight main molecules contributing for more than 5% to the absorption in some wavelength regimes (H_2O, CH_4, CO_2, CO, N_2O, O_2, O_3 and OCS) are indicated in red. Minor contributions are indicated in green: (5) HCN; (7) NO_2; (8) N_2; (10) C_2H_6. Adapted from Smette et al. 2015.

can be mitigated by correcting the spectrum with a computer generated atmospheric model (see Section 4.4), although features in high absorbance regions will be subject to lower signal over noise (S/N) ratio.

Thanks to the relative velocity of the comet, molecular signatures from the comet are Doppler shifted and do not necessarily overlap with their atmospheric counterparts, making it possible to observe cometary emission lines of strong atmospheric absorbers among atmospheric features.

Atmospheric absorptions are the most important features seen in spectra observed from the ground and can be used to precisely calibrate the spectrum wavelength.

3.5 CRIRES

The CRyogenic Infrared Echelle Spectrograph (CRIRES) is a high-resolution spectrograph part of the first generation of the Very Large Telescope (VLT) instruments. It was in operation from 2004 at the European Southern Observatory (ESO) at the Nasmyth A focus of the 8 m telescope VLT-UT1 and later decommissioned in 2014 to be upgraded into CRIRES+, scheduled to be fully operational in 2021.

A summary of CRIRES characteristics is presented in Table 3. CRIRES covers a wavelength range of 0.95 to 5.2 µm, with a resolving power $\lambda/\Delta\lambda$ up to 10^5 with a 0.2 " slit. It can be used with the ESO-MACAO adaptive optics system that corrects the wavefront for atmospheric turbulences in real time, improving the sensitivity by about a factor 2 for point sources (Smoker 2014). It has a footprint of 3 cubic meters for a mass of 6.2 tons.

Calibration system	Halogen lamp, IR-emitter, ThAr, N_2O, CO, visitor gas cells
Adaptive optics	60-actuator curvature sensing MACAO system
Slit length	≈ 40 "
Slit width	From October 1st 2011 two fixed slit widths of 0.2 " and 0.4 "
Echelle grating	40 × 20 cm, 31.6 lines/mm, 63.5° blaze angle
Resolving power	100 000 (0,2" slit); 50 000 (0.4" slit)
Wavelength range	$0.95\ \mu m \leq \lambda \leq 5.2\ \mu m$
Detector science array	4096 × 512 pixels using 4 Aladdin III detectors
Pixel size	27 µm

Table 3: CRIRES spectrograph characteristics. From Smoker 2014.

Functionally, CRIRES can be divided into two part (Smoker 2014; Kaufl et al. 2004). The 'warm' part containing the fore-optics and the adaptative optics system, and the 'cold' part containing the spectrograph itself (Figure 13). The light beam from the telescope (or

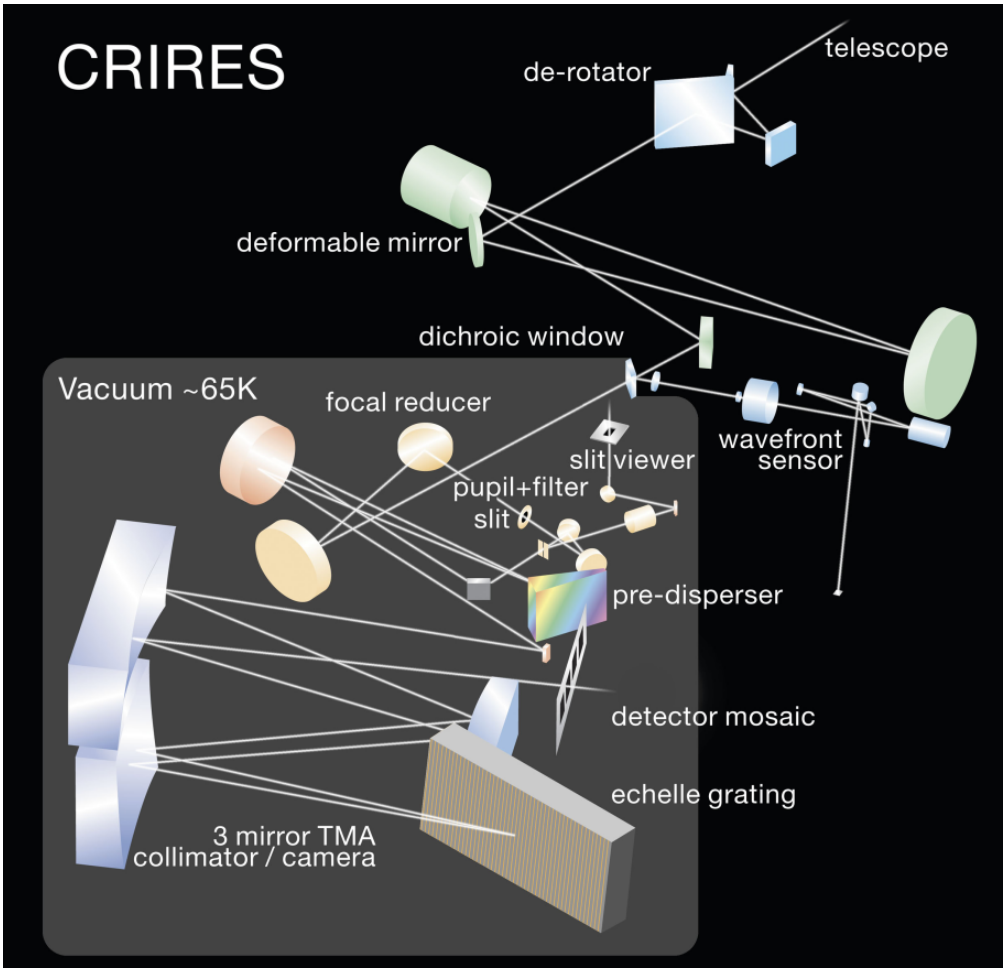

Figure 13: Schema of the CRIRES instrument. The 'cold' part of the instrument is backgrounded in grey. See text for description. From Smoker 2014.

from the wavelength calibration lamp if it is inserted in the light path) enters the warm part of the instrument and first goes through a de-rotator that can optically counteract the effect of the telescope field rotation. The warm part also contains the adaptative optics system. A dichroic window is used to separate the infrared light that is sent to the spectrograph and the visible light that is used by the adaptative optics system.

The 'cold' part is kept under vacuum at ~ 70 K, and down to ~ 27 K for the detectors. The light beam entering the cold part passes through a cold stop, which is an optical device limiting the thermal background, then the slit, and then a pre-disperser prism followed by a medium size slit to reduce the wavelength range before entering the high resolution part of the instrument. A set of mirrors is used to collimate the beam before diffraction by the grating, and as a camera after the diffraction to image the spectrum on the detectors. The detector are four aligned Aladdin 1024 x 1024 pixels InSb detectors, but since only the half

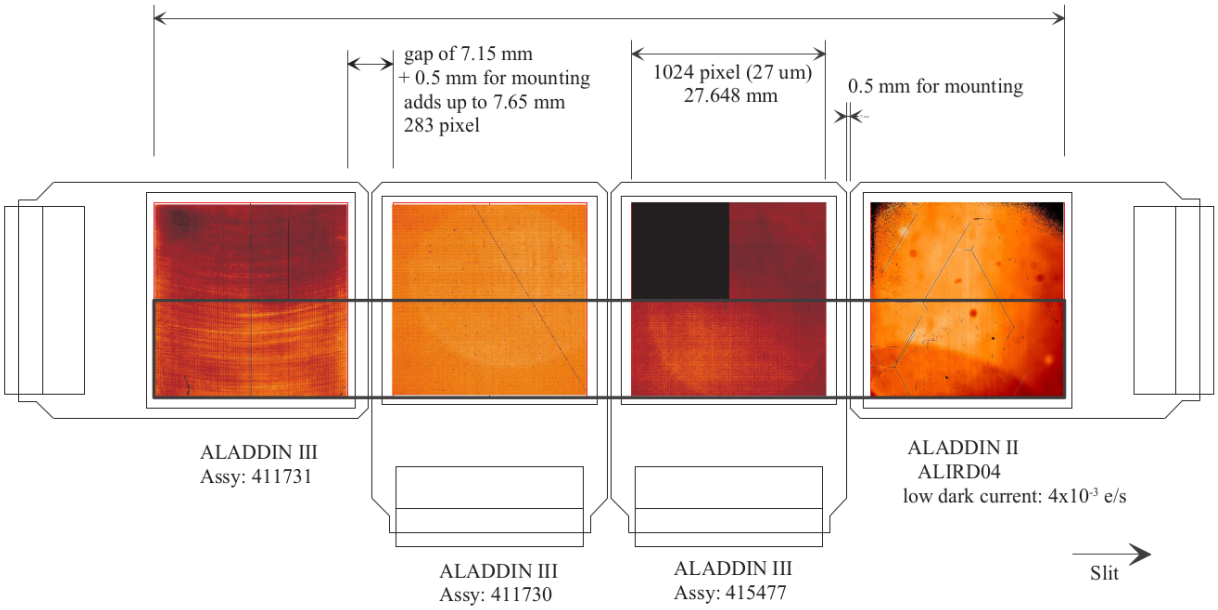

Figure 14: Configuration of the four Aladdin CRIRES detectors. From Moorwood et al. 2003.

lower part is used the totalling pixel array measures 4 x 1024 x 512 pixels (Figure 14). The individual detectors are spaced by the equivalent of ∼280 pixels.

The update into CRIRES+ is meant to transform CRIRES into a cross-dispersed spectrograph to increase the simultaneous spectral coverage by 10 (Dorn et al. 2014; Oliva et al. 2014). Although the spectral resolution of CRIRES is impressive, its wavelength coverage was limited to $\sim 1/70$ of the central wavelength. The modification consists in exchanging the pre-dispersing sub-unit with a cross disperser, that instead of discarding a part of the spectrum before the lights reaches the grating relocates it perpendicularly in regards to the main dispersion direction. The update will also include new Hawaii 2RG detectors, a factor 2.7 larger in the perpendicular direction to the main dispersion, and a new data reduction software.

4 Pipeline for the Infrared Spectroscopy of COmets (PISCO)

4.1 Overview

The main objective of this work is to develop a data processing pipeline that will flawlessly derive meaningful comet characteristics, as the production rates of different chemicals, from raw IR CRIRES data. To this end, a collection of different already existing and newly created tools written in *python3* and *shell script* have been made up into a coherent pipeline named the Pipeline for the Infrared Spectroscopy of COmets (PISCO, Figure 15). Each step of PISCO is more detailed in the following of this section. PISCO is developed with the goal to facilitate the user experience and limit unnecessary setting up of the individual tools by automatically recognising the output files of a given step as the input files of the next one. To this effect, a directory structure to classify the different files is automatically created. The structure also facilitates the storage of different iterations of a given section of the pipeline, which can be reused as input points later on or whose result can be compared to each other. The functionality of already existing tools is sometimes enhanced, for example by building a wrapper around the atmospheric modelling tool MOLECFIT facilitating the use of previously generated model as the starting point of a new fitting. User indispensable interactions are kept to the minimum and sometimes just consists in checking whether the default parameters or results are satisfying. At the end of intermediate steps, the pipeline issues a report for the user and clean now unnecessary files generated to save space on the disk. The ensemble of those tools with their synergy as described here will be refereed to as PISCO, not to be confused with the implemented ESO CRIRES pipeline and ESO MOLECFIT pipeline (the latter also being refereed simply as 'MOLECFIT'). It is a work in progress and the last parts of PISCO are still under development.

4.2 Data acquisition

The different type of images that are used to obtain the final spectrum of the comet are the following:

- science images (Figure 16a): individual frames containing the comet (or reference star) spectra, using the nodding and jittering technique as described below.
- flat fields (Figure 16c): images taken in front of a homogeneous and evenly illuminated source. They allow to correct for shadows produced by the grains of dust, or other

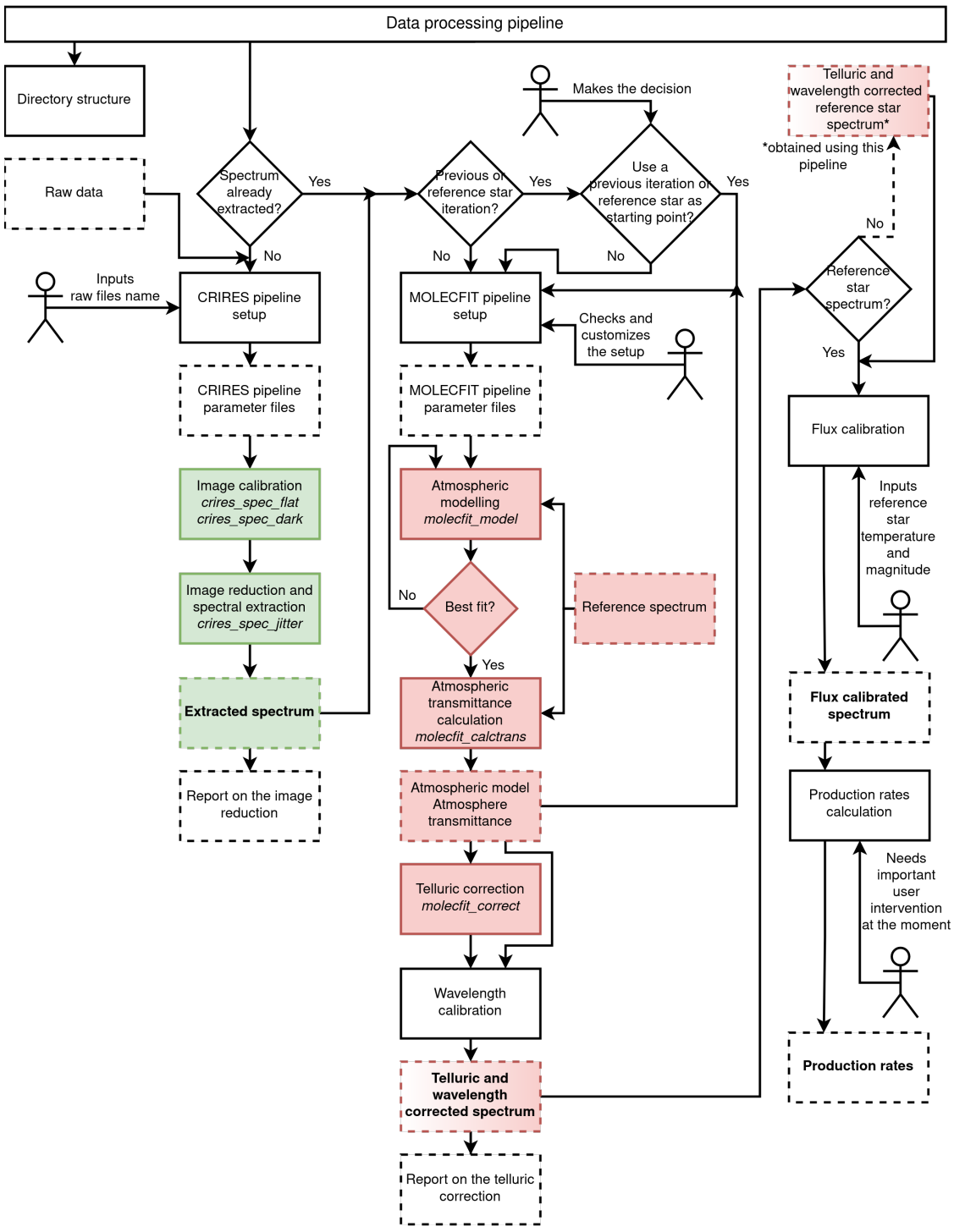

Figure 15: Overview of the PISCO workflow showing the connections between the different elements of the pipeline. Data input and output are encompassed with dashed lines and user inputs are indicated with a stickman. Green and red steps are associated with the CRIRES pipeline and MOLECFIT pipeline, respectively. Each of the steps is described in more details in the text of Section 4.

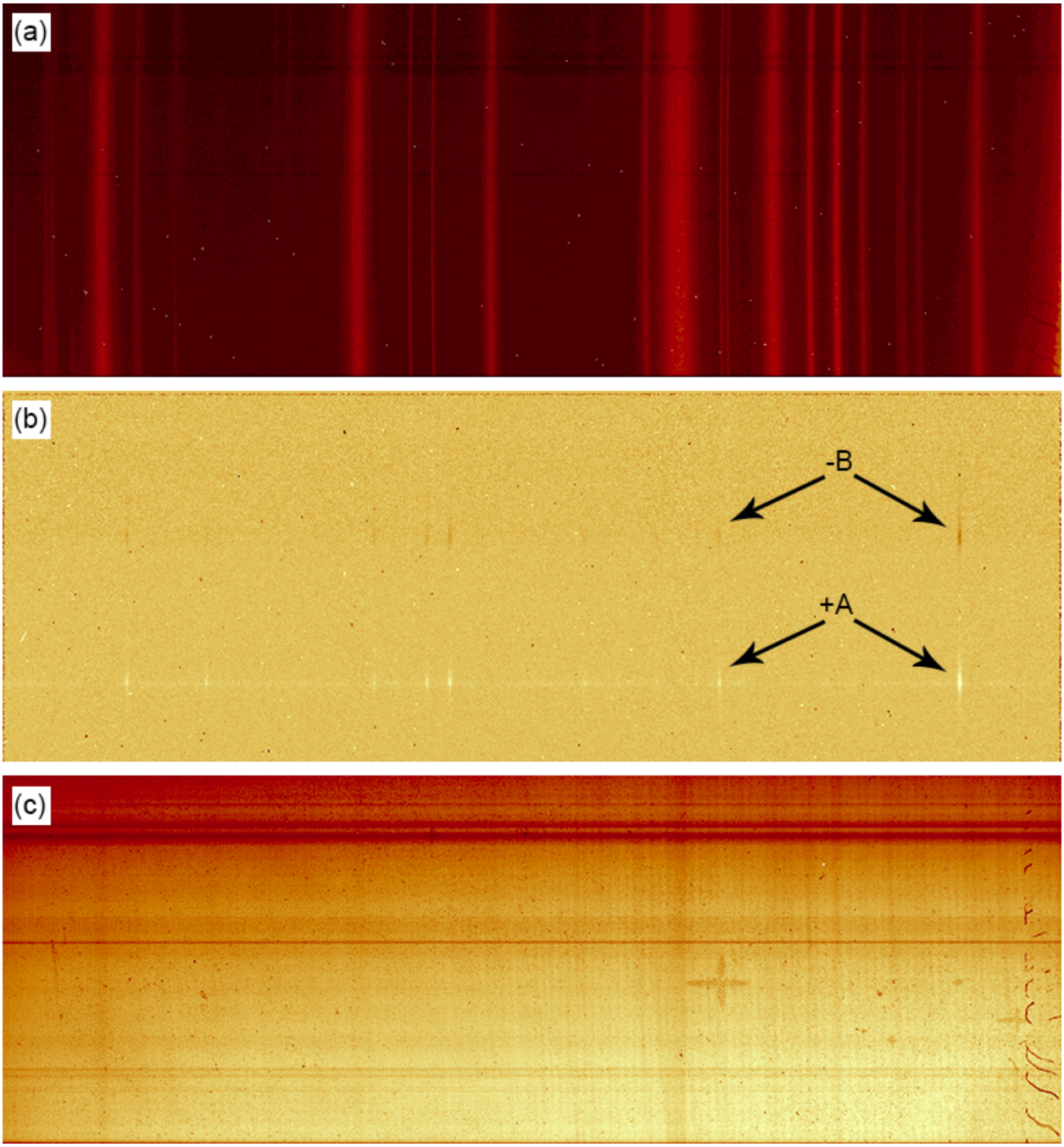

Figure 16: Example of images acquired on the CRIRES detector number 3. (a) Single raw spectrum of a comet observation. Atmospheric signal is clearly visible, but the comet signal is too faint. (b) Image of the detector 3 after compiling individual frames with the nodding and jittering technique and correcting with the master flat by the CRIRES pipeline. Cometary emission lines after the addition of A frames can be seen with a positive intensity on the bottom half of the image (some are indicated by '+A'), and with negative intensity on the upper half of the image from the subtraction of B frames (some are indicated by '-B'). (c) Master flat.

defaults that are in the optical path of the instrument, as well as the pixel to pixel sensitivity variation.

- darks: closed shutter frames recorded with the same exposure time as the image to correct. They record electronic thermal signal.

- detlin files: files containing the non-linearity coefficients of the detectors. They are made available by ESO every 1 or 2 months.

Cometary observations are commonly carried with CRIRES using the nodding and jittering technique (Figure 17). Nodding consists in sequentially taking frames with the comet centered at two different nodding positions along the slit with the same exposure time, first at a position A and then at a position B (Figure 16b, Lippi 2010; Kobayashi et al. 2010). During data processing, subtracting the image B to the image A will cancel the high level background without impacting the comet and telluric signal. To maximise efficiency when the nodding procedure is repeated, image are taken through (A-B-B-A) cycles. Jittering add a random small offset δ_i to the A and B positions for each cycle to avoid the to eventuality of the signal always falling on a same bad pixel on the detector. A typical observing sequence becomes (A-B-B-A'-A'-B'-B'-A"-...) with A'=A+δ_1, B'=B+δ_2, A"=A+δ_3 and so on. The nodding and jittering method is effective to cancel the background noise coming from the IR emission of the telescope and instrumentation, as well as other systematic effects. The bias, an offset added to each pixel when the image is digitized and is usually corrected by a set of no exposure frames with closed shutter, is cancelled as well. The dust continuum resulting

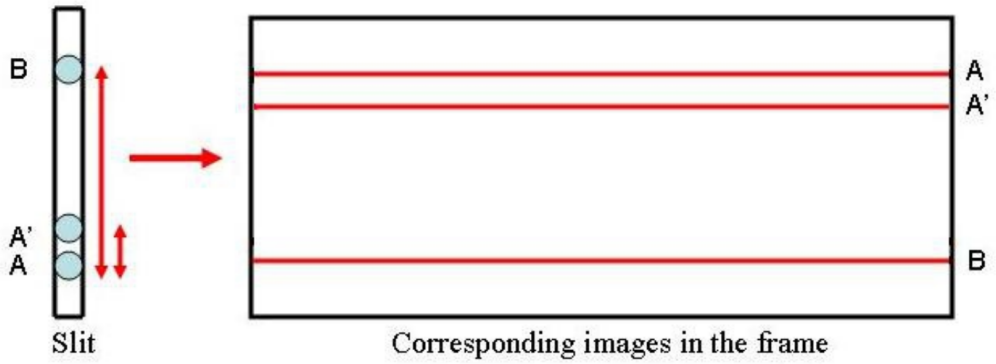

Figure 17: Illustration of the nodding and jittering technique. On the left side, positions of the cometary nucleus on the slit are represented with a blue dot. The vertical arrows represent offset along the slit for nodding (big arrow, from A to B) and jittering (small arrow, from A to A'). On the right, the position of the collected spectrum on the detector is represented for the different nodding and jittering positions. Figure from Lippi 2010.

from the reflection of the infrared radiation of the Sun is not cancelled by the nodding and jittering technique and is a component of the extracted spectrum.

CRIRES images are stored in binary *fits* files containing 5 extensions. The first extension only contains a header with information on the instrument and observational parameters and conditions. Extensions 2 to 5 each contains the image collected on one of the four CRIRES detector and a header with information specific to the detector. In general, the pipelines from ESO that will be described in the next sections replicate this structure for their output files.

4.3 Image reduction: the ESO CRIRES pipeline

4.3.1 Outline

The pre-processing and spectral extraction of the CRIRES images is handled by the ESO CRIRES pipeline[1]. The CRIRES pipeline is organised in different substructures, recipes, that in order to be executed, need to be associated to a *parameter* file as well as a *file input list* file supplied by the user (Smoker et al. 2013).

The master flat frame is computed by combining the individual flat frames, a master dark frame and the detlin files in the ESO CRIRES pipeline *crires_spec_flat* recipe. The master dark frame used to correct the master flat is a compilation of individual dark frames, with the same exposure time as the individual flat frame, computed by the ESO CRIRES pipeline *crires_spec_dark* recipe. The *crires_spec_flat* recipe also computes a bad pixel map used to correct the final image for bad pixels.

The comet spectrum is extracted by inputting the science frames, the master flat and the detlin files into the ESO CRIRES pipeline *crires_spec_jitter* recipe. No master dark is needed to calibrate the science frames since the nodding and jittering method already takes care of cancelling the electronic thermal signal. An important parameter to define is the vertical height (the spatial dimension) over which the spectrum is extracted from the image. A value of 9 pixels centered on the maximum emission is used in this work. It covers well the cometary emissions and is similar to the one used by Kobayashi et al. 2010.

4.3.2 Implementation in the data processing pipeline

The incorporation of the ESO CRIRES pipeline in PISCO is mainly meant to facilitate its execution. *Parameter* and *file input list* files are automatically created for each recipe and the recipes automatically executed. Normally, while writing the *file input list* file, the

[1] https://www.eso.org/sci/software/pipelines/crires/crires-pipe-recipes.html

user should flag each individual file on the list with its type or function, which can be time expensive when there is a lot of different images involved in the spectral extraction. Here, the only input that is asked from the user is the path of the different files, while the flagging is done by PISCO.

Since this is the first step of the data reduction, PISCO also creates a directory structure associated to the dataset. A tidy and systematic storage structure for intermediate files (that will eventually be used later on by PISCO) and end results is necessary to implement results comparison and keep a memory of the parameters used during a previous iteration of a PISCO sub-entity, as well as creating a synergy between the sub-entities that automatically know where their input files are located.

PISCO also plots the result of the spectral extraction and creates a report for the user. Upon a second execution of PISCO with the same dataset, the output files are recognised and the execution of the ESO CRIRES pipeline is skipped by default, which is useful while iterating over other components of PISCO (e.g. when computing a transmittance model from the extracted spectrum).

4.4 Wavelength and telluric lines correction: MOLECFIT

4.4.1 Outline

MOLECFIT[2] is another tool developed by ESO (Smette et al. 2015; Kausch et al. 2015). Absorption of the signal by molecules in the atmosphere is important to take into consideration for ground-based observations, since atmospheric absorption significantly decrease the observed intensity of a comet emission line with respect to its value on the top of the atmosphere. MOLECFIT was developed to correct the spectrum for telluric absorption by using the atmospheric absorptions bands present in the science spectrum continuum itself. As for the ESO CRIRES pipeline, the MOLECFIT functionalities are divided in different recipes that require user supplied *parameter* and *file input list* files to be executed. The procedure executed in MOLECFIT is the fit of a synthetic atmospheric spectrum to the dataset (*molecfit_model* recipe), from which MOLECFIT can compute the atmospheric transmittance (*molecfit_calctrans* recipe). The initial atmospheric profile serving as an input for the calculation of the synthetic atmospheric spectrum is built by MOLECFIT from 3 sources:

- a reference atmospheric profile,
- atmospheric parameters measured at the observatory, encoded in the *fits* file,

[2]https://www.eso.org/sci/software/pipelines/skytools/molecfit

- 3D atmospheric data provided by the Global Data Assimilation System (GDAS) from the National Oceanic and Atmospheric Administration (NOAA) web site[3]

The atmospheric profile contains temperature, pressure and volume mixing ratio of relevant chemical species as a function of the altitude at the time and location of the observation. Those parameters have a direct impact on the shape and size of the telluric lines. MOLECFIT also fetches molecular parameters and lines necessary to calculate the transmission spectrum from the HITRAN database (Rothman et al. 2009), while instrument parameters are retrieved from the *fits* file. It then uses the LNFL/LBLRTM radiative transfer code (Clough et al. 2005) to generate the synthetic spectrum to be fitted to the data with a least-square fitting method. Once a convergence is reached, the science spectrum is corrected by dividing the intensity by the calculated atmospheric transmittance for each wavelength (*molecfit_correct* recipe).

Another possible way to correct for telluric absorption in the science data is to use the spectrum of a reference star with as little as possible intrinsic features, ideally collected during the same night and at the same airmass. If the reference star is approximated to a black body and the only absorption features visible in its spectrum are attributed to the atmosphere, it can easily yield the atmospheric transmittance. Since the spectrum of a standard star is anyway collected for flux calibration (see Section 4.5), it would be an easy alternative to implement. However, using a synthetic spectrum present different advantages (Ulmer-Moll et al. 2019). First, it can save observation time since no reference star needs to be observed. Although in our case a standard star is anyway observed for flux calibration, this is a more general remark. Second, atmospheric parameters can change between the time the science target and the reference star are observed, with possible changes in the transmittance of the atmosphere. Atmospheric water vapour is an important absorber in the 1 to 5 µm region and its atmospheric column can change in short time scales. Not only the time difference is an issue, but also the airmass difference between the two targets that are not at the same position in the sky. The result is a slightly different atmospheric transmission for the comet and reference star spectra.

The synthetic atmospheric model generated by MOLECFIT can also be used to calibrate the wavelength of the science spectrum, although this functionality is not directly implemented in MOLECFIT.

[3]https://www.ready.noaa.gov/gdas1.php

4.4.2 Implementation in the data processing pipeline

As for the ESO CRIRES pipeline, PISCO integrates MOLECFIT by automatically generating the *parameter* and *file input list* files for the different recipes, managing the generated files and generating plots and a report. The parametrisation of the MOLECFIT pipeline, however, is more complex and not always straightforward. Setting up MOLECFIT to have accurate corrections in a reproducible way was probably the most time consuming part of setting up PISCO. Not only because it requires to understand the way MOLECFIT works, but also because modelling the atmosphere is a computer (and time) intensive task.

The *molecfit_model* recipe requires a list of wavelengths intervals, over which the model needs to fit, to be included in the parameter file. Those intervals should exclude non-atmospheric features, like emission lines from the comet. Depending on the spectra, it can be cumbersome to write them by hand and a list of intervals is automatically generated by PISCO (Figure 18). So far in this work, MOLECFIT has shown no difficulty to fit accurately the atmospheric absorbance over all the interval of a detector (with cometary emission lines included), but it may not be the case when a cometary emission lines overlaps strongly with atmospheric features.

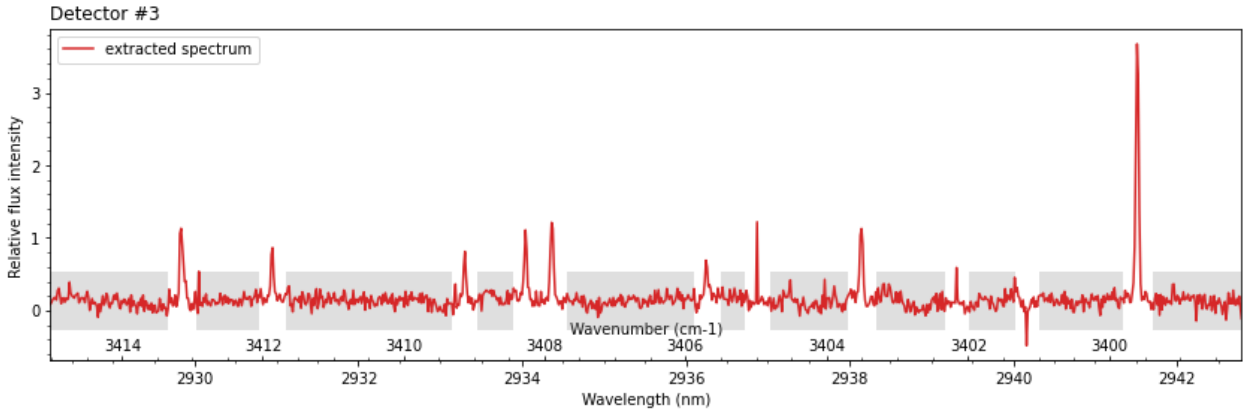

Figure 18: Automatic selection of wavelength ranges by PISCO (highlighted in grey on the spectrum) as inputs for the *molecfit_model* recipe.

Before executing the *molecfit_model* recipe, the initial parameters for the fit are prompted to the user. The parameters defining the CRIRES data format, essential for the recipe to work, are already set up in PISCO and do not require changes by the user. Default values for parameters defining the fit are those proved to work well in the frame of this work, but can be tweaked by the user. The user should, however, select relevant atmospheric molecules to be fit by the model. A most straightforward way to select molecules for the modelling of the synthetic atmospheric spectrum is to generate a transmission spectrum of

the atmosphere that covers the range of the detector with the Planetary Spectrum Generator (PSG, Villanueva, Smith, et al. 2018) web interface[4]. It is more effective than blindly iterating over possible molecules, and more precise than looking at reference spectra that do not have a high resolution. Alternatively, a reference spectrum for atmospheric absorption of different molecules in the 1 to 5 µm region can be found in the Appendix C of the CRIRES user manual (Smoker 2014).

To save computer resources and execution time during debugging of the MOLECFIT integration into PISCO, the processing of only one CRIRES detector (out of the four) at a time, selected by the user, has been implemented. Proceeding this way also saves time when not all detectors show interesting emission lines. Although it should be possible to achieve a single detector selection by setting the working wavelength range on only one detector in the MOLECFIT *parameter* file, this solution has proven to be very unpractical for 2 reasons. First, the ESO MOLECFIT pipeline generates as outputs *fits* files describing the computed model, sized for all the detectors but containing only meaningful information for the one selected. While not being a real problem for the science, this is not practically optimal since an iteration will take 4 times the necessary space on disk. Second and more important, there has been no success in running the next MOLECFIT recipe, *molecfit_calctran*, with this method. Exactly why was not understood, but MOLECFIT issues an error on the content of the output files of the *molecfit_model* recipe, so presumably it could be due to the way the *molecfit_model* recipe writes extension empty of usefull information in the output *fits* file for the detectors that are not fit, as stated above. It is not the goal here to investigates why molecfit does not work, for a workaround has been designed in PISCO. Before the execution of MOLECFIT, the *fits* binary file containing the cometary spectrum with an extension for each of the four detector (the output of the ESO CRIRES pipeline) is rewritten to contain only one extension with the spectrum of the detector of interest, solving the issues presented above.

PISCO does not only execute MOLECFIT and prepare the files necessary to its execution, it also consists of a framework facilitating the use of most advanced functions of MOLECFIT. PISCO saves the results from previous MOLECFIT iterations and prompt the user with the choice of using a previous model as an input for the next iteration. While setting up MOLECFIT for the comet observation, if the correction for the standard star from the same dataset as the comet has already been computed, the user can choose to use the standard star model as an input. The user has also the option to directly apply the correction from the standard star to the comet, which can be useful if the continuum of the comet is too faint, preventing for a good modelling of the atmosphere transmittance, but comes with the

[4]https://psg.gsfc.nasa.gov/

risk of applying a slightly offset correction as discussed above.

Finally, applying directly a wavelength correction is not implemented in MOLECFIT, although the wavelength from the atmospheric synthetic spectra can be found in the output files of the *molecfit_calctran* recipe. The wavelength correction for comet and reference star spectra is applied by PISCO.

4.5 Flux calibration

The intensity of the spectra is until this point expressed with instrumental related values ([ADU s^{-1}] for a given wavelength), but it can be converted into the corresponding flux density ([W m^{-2} nm^{-1}]) if a standard star with a known flux in the IR is observed with the same instrumental configuration as the science target. The standard star spectrum is extracted and corrected for the wavelength and the telluric lines the same way as the comet spectrum with PISCO. We follow here the process described in Bonev 2005 for the flux calibration.

For each wavelength, a conversion factor $\Gamma(\lambda)$ between the directly measured instrumental counts per unit time and their corresponding flux density is obtained from:

$$\Gamma(\lambda) = \frac{f_{star}(\lambda)}{COUNTS(\lambda)/t \cdot F_{cor}} \qquad [\text{W m}^{-2}\ \text{nm}^{-1}\ (\text{ADU/s})^{-1}] \tag{18}$$

where $f_{star}(\lambda)$ is the predicted flux density of the IR standard star, $COUNTS(\lambda)/t$ is the measured intensity in instrumental related values and F_{cor} a correction for slit loss. F_{cor} is the ratio between the predicted counts for an infinitely wide slit and the measured counts for the real slit. The IR standard star is usually observed with the widest slit available in order to maximise F_{cor}.

The first step to calculate $f_{star}(\lambda)$ is to convert the published magnitude m of the IR standard star for the effective center wavelength λ_0 of a given IR band into flux density using the standard magnitude-flux relation with Vega (α-Lyrae) as the zero magnitude reference:

$$f_{star,\lambda_0} = f_{m=0,\lambda_0} \cdot 10^{-0.4m} \tag{19}$$

In the frame of this work, m has been chosen to be the magnitude in the L band (centered at 3547 nm) of the IR standard star. The value of m can be retrieved in IR standard star catalogues published by observatories such as the UKIRT Bright Standards[5] or a more general catalogue like SIMBAD[6]. $f_{m=0,\lambda_0}$ is the flux of Vega at λ_0, a value of

[5]http://www.not.iac.es/instruments/notcam/ReferenceInfo/ukirt_stds.html
[6]http://simbad.u-strasbg.fr/simbad/

$6.590 \cdot 10^{-14}$ W m^{-2} nm^{-1} at 3547 nm (Cohen et al. 1992) is used in this work.

$f_{star}(\lambda)$ is derived via the Planck function at a temperature approximating the stellar spectral class T_{star} by

$$f_{star}(\lambda) = f_{star,\lambda_0} \frac{B(\lambda, T_{star})}{B(\lambda_0, T_{star})} \tag{20}$$

The stellar class can be found in the same star catalogue as the reference magnitude, while a useful table to get T_{star} from the stellar class is given by Landon Curt Noll's website[7]. $B(\lambda, T)$ is the Planck function for the spectral radiance of a given object at a temperature T and a wavelength λ and is expressed as

$$B(\lambda, T) = \frac{2hc^2}{\lambda^5} \frac{1}{e^{hc/\lambda k_B T} - 1} \qquad [\text{W sr}^{-1} \text{ m}^{-2} \text{ nm}^{-1}] \tag{21}$$

Flux calibration is implemented into PISCO as described above. The used only needs to input the properties of the reference star, that is m and T_{star}.

4.6 Emission lines identification

Attribution of the emission lines to molecules is done manually with the help of the HITRAN online database[8] (Hill et al. 2016) and some of the published work refereed to in Section 5.

4.7 Line-by-line flux calculation

With the spectrum calibrated, the flux for a given line is retrieved by integrating the flux density over the emission line. Since there is no automatic line identification, the user needs to select the wavelength of the line. PISCO uses the Gaussian fitting library from the astropy package[9].

4.8 Production rates

The way to derive the production rate Q_i for an individual transition i is partially described in Section 3.2. The measured flux F_i can be related to the molecular column density through the emission rate g_i for the transition i (see Equation 15), and the spatial distribution and dynamic of the column density needs to be modelled to relate the density to the production rate, e.g. with the Haser model (see Equation 16). In overall, the production rate is related

[7] http://www.isthe.com/chongo/tech/astro/HR-temp-mass-table-bytemp.html
[8] https://hitran.org/
[9] https://www.astropy.org/

to the flux by the emission rate:

$$Q_i \propto \frac{F_i}{g_i} \tag{22}$$

The emission rate g_i can be defined as the product between the spontaneous emission Einstein coefficient for the i transition and the fractional population of the corresponding upper level (Bonev 2005). Deriving g_i requires to build a fluorescence model for the molecule of interest as well as retrieving the specie rotational temperature T_{rot} from the intensity ratio and shape of individual rotational lines in the spectrum. T_{rot} is an important parameter related to the distribution of the population among the ro-vibrational energy levels. It is common to assume that the different species in the comet coma have a similar T_{rot} and use the T_{rot} measured for H_2O to calculate the production rates of all the other species during the same night. Once the production rate has been derived for each of its individual line, the overall production rate for a specie can be derived as a weighted mean of line-by-line measurements.

Unfortunately, in the time frame of this work, it has not been possible to implement a complex procedure like the one described above. In order to be able to show the end result of a complete CRIRES dataset processing yielding the comet production rates in this work, an alternative but less robust way to derive them using the PSG web interface and published T_{rot} is adopted. PSG has the capability of producing a synthetic spectrum of a comet with interesting freedom in the parametrisation of the comet model and the instrumental parameters used to calculate the spectrum. More importantly, the chemistry of the volatiles in the comet model is rich enough for our purpose, with a range of parent molecules whose activity and temperature can be configured (Villanueva, Mumma, et al. 2012; Villanueva, Magee-Sauer, and Mumma 2013). The approach taken here is to fix the rotational temperature and the production rate of the comet in the PSG model with values taken from the literature to generate a fluorescence model. The synthesised fluorescence spectrum is then downloaded to be fed into a home-made script that calculates the line fluxes. From Equation 22, for a given line, the ratio between the flux from the model $F_{PSG}(T_{rot})$ and the observed flux F_i is equal to the ratio between the production rate fixed in the model Q_{PSG} and the production rate for the observed line Q_i, allowing to calculate Q_i by

$$Q_i = Q_{PSG} \frac{F_i}{F_{PSG}(T_{rot})} \tag{23}$$

It is important to note that T_{rot} used in the model is not obtained from the observation dataset using this method.

4.9 Discussion on PISCO

PISCO effectively synergies different publicly available and home-made tools, making their use faster and easier than if they were used separately. It is not, however, as flawless as aspired when introducing the idea in Section 4.1 and still needs development. This is mostly true for the production rates calculation that is not yet fully implemented. Automating this step would require to build a quantum model for the molecule, which is not trivial. The workaround presented in this work relies on calculating of fluxes derived from PSG models for each line and values of T_{rot} from the literature. An intermediate solution worth investigating to reduce the complexity of the implementation of a modelling tool in PISCO while allowing automation of data processing is to use the PSG Application Program Interface (API). The PSG API could also be used to automate the selection of atmospheric molecules to fit while setting up MOLECFIT.

PSG is an interesting tool which could be an alternative to MOLECFIT for generating a transmission spectrum. The reason for developing PISCO around MOLECFIT for telluric and wavelength corrections in the first place is because it is an ESO developed tool that may be implemented natively into the CRIRES+ and METIS data reduction pipelines (METIS will be one of the Extremely Large Telescope instrument, see Brandl et al. 2021 for a description). Those instruments promise to deliver among the best comet ground-based IR observations in terms of sensitivity and resolution in the next decade. Getting familiar with this specific tool is therefore completely in line with the objective of developing comet IR capabilities in Liege. In overall, once set up properly, MOLECFIT has shown good results with correcting the datasets while tested during the development of PISCO, except in one dataset where the continuum was too weak to calculate and accurate transmission spectrum.

Partially relying on external tools has its perks and cons. The biggest advantage is obviously not having to develop complex tools and reinvent the wheel. Widespread use of a tool can also facilitate data comparison between different studies. The downside is that depending on the amount of documentation available, they can behave as a 'black box' where the user has no real understanding of how things work, which can complicate troubleshooting if the tool is not performing as expected. It has been experienced to a certain degree while implementing the ESO CRIRES and ESO MOLECFIT pipelines into PISCO and while using PSG.

The potential of PISCO is practically demonstrated in Section 5 where it is used to process a CRIRES observation of 8P/Tuttle.

5 Science case: the 8P/Tuttle 2008 perihelion

5.1 The 8P/Tuttle comet

8P/Tuttle is a periodic Halley type comet ($T_J < 2$ and $a < 40$ AU, see Section2.2) with a periodicity of 13.6 years. Its orbital properties are presented in Table 4. The comet was discovered independently by Horace Parnell Tuttle in the USA on January 4, 1858, and Karl Christian Bruhns in Germany on January 11 of the same year. The first calculations of the comet orbit revealed that it was the same comet discovered by Méchain in France on January 9, 1790, but whose intensity was fainter and orbital parameters poorly constrained at the time (Kronk, Meyer, and Seargent 1999).

Period	13.61 years
Eccentricity	0.81
Semi-major axis	5.70 AU
Inclination	54.98 degrees
Aphelion distance	10.38 AU
Last perihelion*	2008 January 27
Next perihelion*	2021 August 27

Table 4: Orbital parameters of 8P/Tuttle. Retrieved from the JPL Small-Body Database Browser[11]. More accurate values and uncertainties are available in the JPL database. *at the time of writing.

Conditions were especially favourable to study the comet during its 2007-2008 visit to the inner solar system with the closest approach to the Earth on the 1st of January 2008 at a distance of 0.25 AU just before its perihelion on the 27th of January (Figure 19 lower left) at a distance of 0.52 AU from the Earth. The next perihelion is on 2021 August 27 (Figure 19 upper left) is at a distance from the Earth of 1.84 AU and on the opposite side of the Sun, and is not a favourable perihelion for observation. The next visit with a close encounter comparable to 2008 will be only in December 2048[12].

[11] https://ssd.jpl.nasa.gov/sbdb.cgi

[12] Comet ephemeris can be found at the NASA HORIZONS web interface at https://ssd.jpl.nasa.gov/horizons.cgi

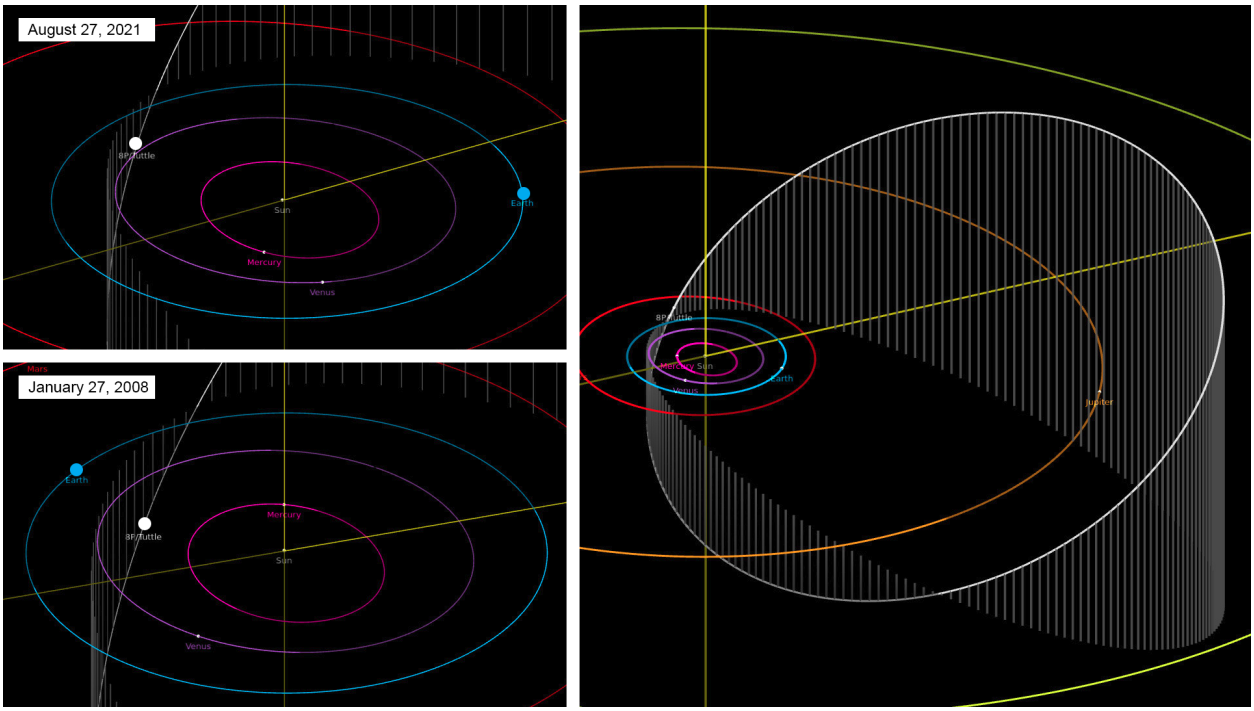

Figure 19: 8P/Tuttle orbit and position in the solar system at the 2008 and 2021 perihelion. The orbit of 8P/Tuttle is represented in white, of the Earth in blue and of Jupiter in orange. The right image shows the entire 13.61 years orbit of 8P/Tuttle. The left upper and lower images are zooms on the inner part of the solar system configuration on August 27, 2021 (next 8P/Tuttle perihelion), and January 27, 2008 (last 8P/Tuttle perihelion), respectively. Source images generated by the JPL Small-Body Database Browser.

5.2 Selected dataset

The CRIRES 8P/Tuttle data used here are the same used and described by Kobayashi et al. 2010 (ESO Programme 280.C-5053). In this work, two settings containing H_2O and HCN lines, observed on January 27, 2008, and two settings containing H_2O, CH_4 and C_2H_6 lines, observed on February 4, 2008, are analysed (see Table 5). The raw images of the comet and of the standard star were retrieved from the ESO public archive[13] along with the corresponding calibration images (dark, flat and detlin). Only one flat field image per observation night was available in the archive. The comet and the standard star were observed with a 0.2" and 1.0" wide slit, respectively, and 31" large. The standard star for both nights was 30 Monocerotis, a A0V class star with a L magnitude $m_L = 3.94$ and a color temperature $T_{star} = 9900$ K.

[13] http://archive.eso.org/eso/eso_archive_main.html

Date	Time [UT]	Molecules	Wavelength coverage [nm]	d_S [AU]	d_E [AU]	v_r [km/s]	Airmass
Jan 28, 2008	1:28−2:47	HCN	3000.8−3064.3	1.027	0.523	24.798	1.36
	3:13−4:07	H_2O	2888.1−2961.2	1.027	0.524	24.865	2.03
Feb 4, 2008	0:49−1:54	H_2O	2935.8−3005.1	1.035	0.621	24.187	1.27
	2:20−3:23	CH_4, C_2H_6	3244.8−3362.2	1.035	0.622	24.252	2.52

Table 5: Overview of CRIRES observations made by Kobayashi et al. 2010 used in this work. d_S, d_E, and v_r are the heliocentric distance, geocentric distance and topocentric velocity of the comet, respectively, at the midpoint of the time interval. All comet observations were taken with a 0.2" slit.

5.3 Results and discussion

5.3.1 Spectral extractions, corrections and calibrations

All the datasets were processed using PISCO for the comet and the standard star as described in Section 4.

The extracted spectrum with its atmospheric model fitting on detector #3 for the January 27 H_2O setting is presented in Figure 20 for the comet and Figure 21 for the standard star. Those plots (except the annotations) are build inside PISCO as part of the automatically generated reports. H_2O is the only significant atmospheric absorber in this wavelength range. To appreciate the precision of the transmittance calculation from the comet spectrum continuum, even when it is weak, the transmittance derived from the comet continuum can be compared to the transmittance derived from the standard star. Indeed, if we consider that the emission of the standard star does not have any intrinsic feature and that its flux is constant over the wavelength range, the resulting observed spectrum contains only telluric features with a high S/N ratio. The computed transmittance should therefore be very similar to the star spectrum, which indeed is the case (first and third panel of Figure 21). When the transmittance computed from the standard star spectrum is compared to the transmittance computed from the comet continuum (third panel in Figure 20), we can see that they are almost similar. All the telluric lines are found at the same wavelength, and the overall aspect of the transmittance spectrum is similar over all the wavelength range. Features in the transmittance spectrum from the comet are also 'sharp' (the Gaussian component of the telluric lines is exaggerated when MOLECFIT cannot well constrain column densities, as will be discussed with the HCN setting). The transmittance is slightly higher for the comet observation, which can be explained by a more important column density of H_2O in the atmosphere compared to the standard star, from a combination of changes in atmospheric conditions during the night and a different airmass. The water column density variation

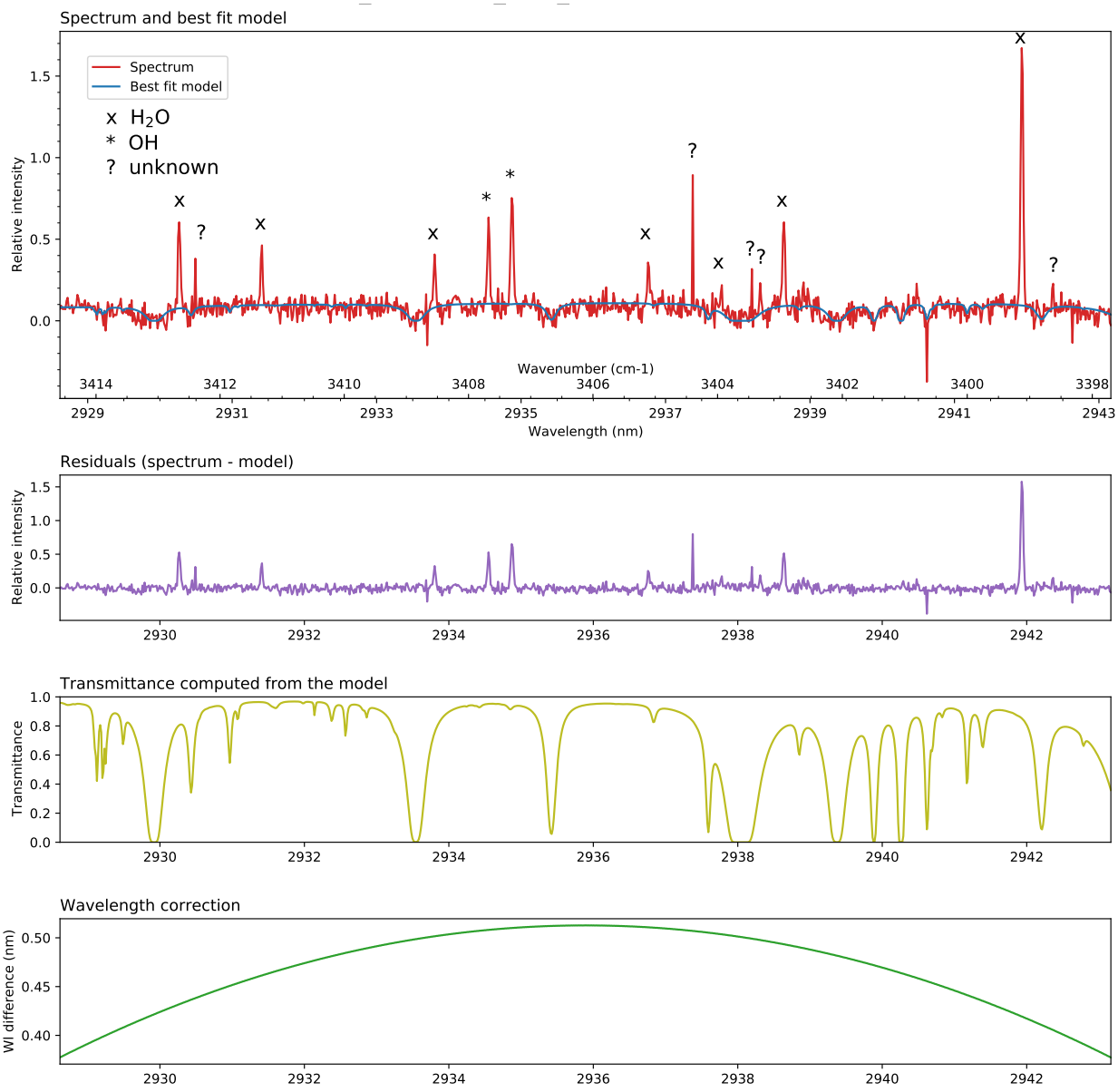

Figure 20: 8P/Tuttle spectrum extracted for the CRIRES detector #3 with the January 27 H_2O setting and results of the MOLECFIT atmospheric model fitting. From top to bottom: the first panel shows the extracted spectrum in red and the best fit of the continuum in blue. The second panel is the residual from the fit. The third and fourth panels are the atmospheric transmittance and the wavelength correction, respectively, calculated by MOLECFIT from the fit of the continuum.

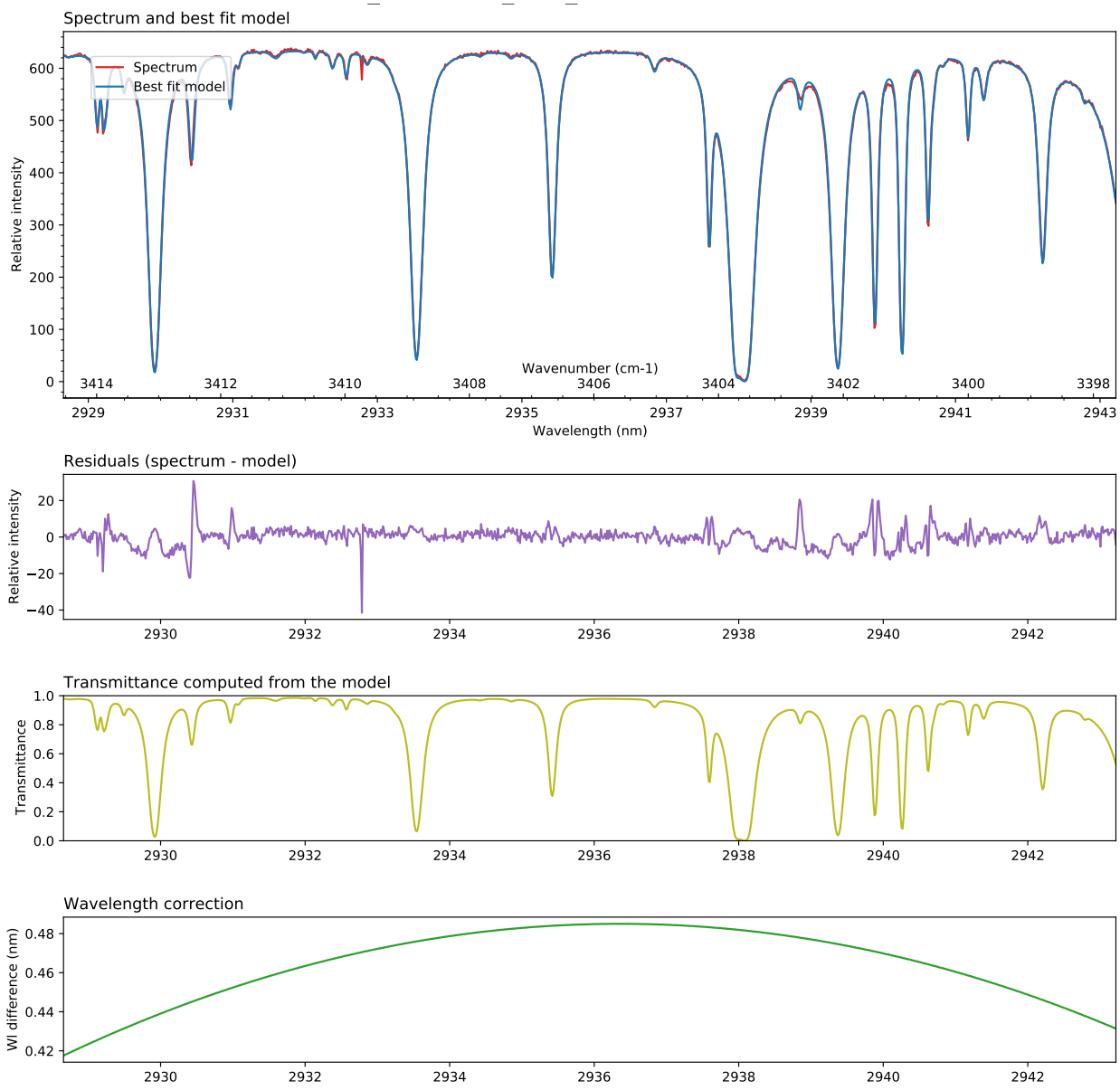

Figure 21: Standard star spectrum extracted for the CRIRES detector #3 with the January 27 H_2O setting and results of the MOLECFIT atmospheric model fitting. See Figure 20 caption for the description of the different panels.

highlights the advantage of correcting for telluric features from the comet continuum rather than using a reference star. The wavelength correction for both observations has the same trend and is similar within 0.05 nm.

Spectra for other selected settings are presented in Figure 22. For the HCN setting, the fitting of the atmospheric model is of inferior quality compared to the H_2O setting presented in Figure 20. The computed transmittance shows a broadening of the telluric features (Figure 22 top). Although the continuum is stronger than for the H_2O setting, the S/N ratio is smaller. This lower S/N ratio could be the reason for which MOLECFIT is struggling to accurately describe finer telluric features. Fortunately, HCN is not an important absorber in the atmosphere and HCN emissions from the comet are not overlapping with important telluric lines. In high transmission regions, the inaccuracy of the telluric correction caused by the broadening of the transmittance model features should be minimal.

As mentioned before, only one flat field correction frame could be retrieved per observation night. It is possible that more flat frames were taken outside of the official program for technical reasons and not included in the archive. It is desirable to combine different flat frames into a master flat. It has the advantage of reducing the noise of the produced master flat, preventing an unwanted increase of noise in the reduced science image when it is divided by the master flat by the ESO CRIRES pipeline. The flat field correction has proven to be a problem when trying to identify the C_2H_6 cometary emission lines. While C_2H_6 emission lines are detected at their expected position in the extracted spectrum without flat field correction (Figure 22 top in red), they are not when the flat field correction is applied (Figure 22 bottom in blue). An increase of the noise in the corrected spectrum is appreciable as well. Therefore, no flat field correction was applied to the C_2H_6 setting before calculating the lines flux in this work.

CH_4 lines, whose detection is reported by Kobayashi et al. 2010 (very faint, in the same dataset), Böhnhardt et al. 2008 (January 26 and January 27, 2008, with CRIRES), and Bonev et al. 2008 (December 22–23, 2007, with NIRSPEC at Keck 2) could not be unambiguously identified here, with or without flat field correction. A likely explanation for the non-detection in this work is a less effective way to reduce the noise during the data reduction. This explanation is supported by the more important number of lines at a weaker flux reported by Kobayashi et al. 2010 than what could be identified here for identified molecules in the same dataset.

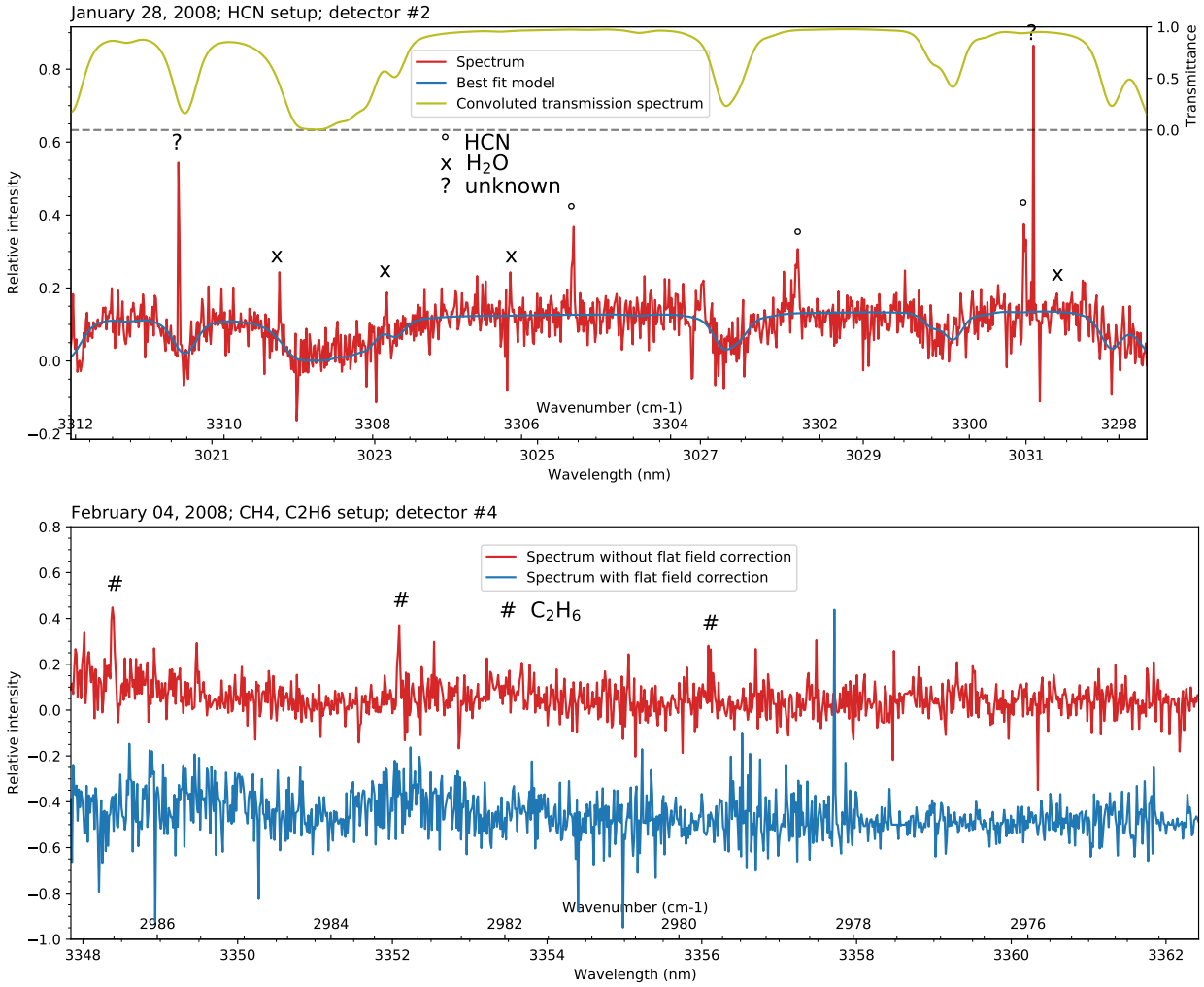

Figure 22: Selected spectra of 8P/Tuttle. Top: spectrum of HCN (red) observed on January 28, 2008 (detector #2) and the calculated transmittance (green, scale on the right). Bottom: spectrum of C_2H_6 observed on February 04, 2008 (detector #4). The blue and red spectra are the same dataset processed with and without flat field correction, respectively. The blue spectrum is shifted by -0.5 on the y axis.

5.3.2 Production rates and mixing ratios

Calculated fluxes for the identified lines in the observations described in Table 5 are presented in Tables 6 to 9, along with the fluxes reported by Kobayashi et al. 2010 for the same dataset. A slit correction factor of 1 was assumed for the standard star (a good approximation for a point source, if the slit is wide, and the seeing good). Calculations of the flux losses for the comet were incorporated into the PSG fluorescence model. With few exceptions, fluxes calculated in this work and by Kobayashi et al. 2010 are consistent within their uncertainties. For all flux values, the uncertainties are larger in this work than those Kobayashi et al. 2010, which is expected as we have a lower S/N ratio. Nevertheless, for some individual lines, the uncertainties are overestimated. Uncertainties are given by the Gaussian fit of the individual lines and are dependant on the noise level surrounding the line. The script for the Gaussian fitting used in PISCO does not recognise other emission lines in the fitting range and therefore consider them the same way as noise regarding the uncertainty calculation, resulting in an overestimation of the uncertainty. This is the case for example for the HCN 3030.74 nm transition (Table 7) that has a calculated flux and a large uncertainty of $(8.08 \pm 4.97) \times 10^{-20}$. An overestimation of the uncertainty can also occur when the range considered for the Gaussian fit contains a region with low atmospheric transmittance. Even if the line is not in the low transmittance region but just next to it, the calculation of the uncertainty will be affected by the inherent higher noise of the low transmittance region. This unwanted behaviour of PISCO has yet to be corrected. For this reason, plots of the lines fit over the interval for which the uncertainty was calculated are made available for each line in Appendix A.

Another anomaly is the calculated flux of the 3348.14 nm C_2H_6 line (Table 9) that is more than 3 times higher than the reported one. As discussed above, the spectrum of the C_2H_6 setting was not flat field corrected because the correction had the undesirable side effect of increasing the S/N ratio, making the emission lines disappear in the noise. Given that the line was well visible in the uncorrected spectrum (Figure 22 bottom), it is probable that the flat field correction not only added the undesirable noise but also decreased the intensity in that region. The abnormally high flux value for the 3348.14 nm C_2H_6 line therefore could be an instrument induced effect left uncorrected.

Aside from those last considerations, obtaining flux values coherent with those published by Kobayashi et al. 2010 is an encouraging result that demonstrates that on the whole PISCO performs correctly.

Production rates and mixing ratios (the ratio between a given molecule and the water production rates, in percent) are presented in Table 10 and Table 11, respectively. This work uses the rotational temperatures derived by Kobayashi et al. 2010 (see Table 10) as

Transition* Wavelength [nm]	Observed* Wavelength [nm]	Flux [W m^{-2}] This work	Flux** [W m^{-2}] Kobayashi et al. 2010
2930.04	2930.23	$(1.53 \pm 0.23) \times 10^{-19}$	$(1.10 \pm 0.08) \times 10^{-19}$ [0.80]
2931.16	2931.41	$(7.67 \pm 0.92) \times 10^{-20}$	$(7.92 \pm 0.66) \times 10^{-20}$ [0.94]
2936.49	2936.76	$(8.12 \pm 1.67) \times 10^{-20}$	$(5.98 \pm 0.72) \times 10^{-20}$ [0.91]
2938.38	2938.64	$(1.54 \pm 0.23) \times 10^{-19}$	$(1.26 \pm 0.09) \times 10^{-19}$ [0.76]
2941.72	2941.93	$(4.26 \pm 0.16) \times 10^{-19}$	$(4.01 \pm 0.08) \times 10^{-20}$ [0.82]
2950.92	2951.24	$(9.26 \pm 1.27) \times 10^{-20}$	$(8.34 \pm 0.66) \times 10^{-20}$ [0.94]
2956.74	2957.03	$(4.51 \pm 0.16) \times 10^{-19}$	$(3.79 \pm 0.07) \times 10^{-19}$ [0.89]
2959.91	2960.13	$(9.38 \pm 2.36) \times 10^{-20}$	$(9.53 \pm 0.76) \times 10^{-20}$ [0.75]

Table 6: 28 January 2008, $\mathbf{H_2O}$ lines identification and their calculated flux. *The transition wavelength is the theoretical value for the transition; the observed wavelength is Doppler shifted from the transition wavelength due to the relative velocity of the comet. **The flux from Kobayashi et al. 2010 is presented without atmospheric correction, unlike the flux from this work that is corrected for telluric absorption. For this reason, the atmospheric transmittance calculated by Kobayashi et al. 2010 is indicated between brackets for each transition.

Transition* Wavelength [nm]	Observed* Wavelength [nm]	Flux [W m^{-2}] This work	Flux** [W m^{-2}] Kobayashi et al. 2010
3004.11	3004.35	$(4.26 \pm 1.20) \times 10^{-20}$	$(4.22 \pm 0.58) \times 10^{-20}$ [0.94]
3006.66	3006.92	$(7.78 \pm 2.07) \times 10^{-20}$	$(5.77 \pm 1.37) \times 10^{-20}$ [0.90]
3014.47	3014.75	$(4.76 \pm 1.95) \times 10^{-20}$	$(3.43 \pm 1.27) \times 10^{-20}$ [0.86]
3025.22	3025.44	$(6.40 \pm 1.48) \times 10^{-20}$	$(7.12 \pm 0.73) \times 10^{-20}$ [0.96]
3027.92	3028.19	$(7.79 \pm 1.90) \times 10^{-20}$	$(7.85 \pm 0.89) \times 10^{-20}$ [0.96]
3030.74	3030.98	$(8.08 \pm 4.97) \times 10^{-20}$	$(7.40 \pm 0.81) \times 10^{-20}$ [0.93]

Table 7: 28 January 2008, **HCN** lines identification and their calculated flux. *,** See Table 6 caption.

Transition* Wavelength [nm]	Observed* Wavelength [nm]	Flux [W m^{-2}] This work	Flux** [W m^{-2}] Kobayashi et al. 2010
2938.38	2938.66	$(8.86 \pm 5.05) \times 10^{-20}$	$(6.84 \pm 0.77) \times 10^{-20}$ [0.64]
2941.72	2941.92	$(4.60 \pm 0.89) \times 10^{-19}$	$(1.98 \pm 0.06) \times 10^{-19}$ [0.74]

Table 8: 04 February 2008, $\mathbf{H_2O}$ lines identification and their calculated flux. *,** See Table 6 caption.

Transition* Wavelength [nm]	Observed* Wavelength [nm]	Flux [W m^{-2}] This work	Flux** [W m^{-2}] Kobayashi et al. 2010
3348.14	3348.42	$(1.41 \pm 0.41) \times 10^{-19}$	$(4.23 \pm 0.60) \times 10^{-20}$ [0.91]
3351.90	3353.18	$(6.41 \pm 2.71) \times 10^{-20}$	$(4.51 \pm 0.60) \times 10^{-20}$ [0.94]
3359.35	3359.60	$(3.19 \pm 1.96) \times 10^{-20}$	$(2.58 \pm 0.71) \times 10^{-20}$ [0.91]

Table 9: 04 February 2008, $\mathbf{C_2H_6}$ lines identification and their calculated flux. *,** See Table 6 caption.

input into a fluorescence model for each molecule computed by PSG in order to derive the production rates, as described in Section 4.8. The values presented are averages of individual production rates, or mixing ratios, for individual lines. Uncertainties in production rates and mixing ratios are dominated by systematic uncertainties, e.g. uncertainties from the transmittance and the fluorescence models, and not by the stochastic noise of the sky-background (Kobayashi et al. 2010). The uncertainty presented is the standard deviation of the production rates, or mixing ratios, over the population of averaged lines. The number of lines sampled for each setting is also indicated in Table 10. The production rates of H_2O, for both observing nights, and of HCN are consistent with the production rates found by Kobayashi et al. 2010 within their uncertainties. Only an upper value for the production rate of C_2H_6 could be constrained due to the poor quality of the flux calculations of the C_2H_6 lines, as explained above. The mixing ratio of HCN (see Table 11) is consistent with the work of Kobayashi et al. 2010, as well as the work of Bonev et al. 2008 that observed 8P/Tuttle with NIRSPEC at the Keck Observatory in Hawaii in December 22-23, 2007. Like for the production rate, only an upper value of the mixing ratio of C_2H_6 could be found.

In the end, this demonstrates that PSG can be a good tool to calculate the production rates, given that T_{rot} is known, or at least that the PSG model is in agreement with models used by Kobayashi et al. 2010 and Bonev et al. 2008. Nevertheless, T_{rot} is a major parameter of the fluorescence model. Therefore, deriving it from the data should be a prime focus in the future development of PISCO.

Molecule	This work		Kobayashi et al. 2010		
(date)	# Lines	Q [10^{-28} s^{-1}]	# Lines	Q [10^{-28} s^{-1}]	T_{rot} [K]
H_2O (28/01)	8	4.32 ± 1.7	25	4.6 ± 0.4	70 ± 15
HCN (28/01)	6	$(3.18 \pm 1.35) \times 10^{-3}$	11	$(3.4 \pm 1.1) \times 10^{-3}$	54 ± 9
H_2O (04/02)	2	3.50 ± 0.21	15	3.0 ± 0.2	65^{+15}_{-13}
C_2H_6 (04/02)	3	$< 4.21 \times 10^{-2}$	4	$(6.7 \pm 1.3) \times 10^{-3}$	70*

Table 10: Production rates Q of 8P/Tuttle. # Lines indicates the number of individual lines averaged to calculate the production rate. * T_{rot} from H_2O (28/01) was used to calculate the production rate of C_2H_6.

Molecule	This work	Kobayashi et al. 2010	Böhnhardt et al. 2008	Bonev et al. 2008
HCN	0.07 ± 0.3	0.07 ± 0.02		0.07 ± 0.01
C_2H_6	< 1.21	0.23 ± 0.04	(26/01) 0.30 ± 0.03	0.24 ± 0.03
			(27/01) 0.28 ± 0.06	

Table 11: 8P/Tuttle mixing ratios [%, with water at 100%] measured during the 2007-2008 apparition.

6 Conclusion

Comets have always been mysterious objects. In past History, their fiery and unpredictable appearances in the sky could shake entire civilisations as they were interpreted as heavenly and often evil omens, and even served as instrument of political power. Today, while investigated with modern scientific instruments, they still keep valuable secrets. They could be the key to a more profound understanding of the solar system formation and evolution, they could have filled the Earth's oceans with their water, or even could have brought prebiotic chemistry on Earth. A better understanding of their chemistry is required to elucidate those fundamental points.

Parent and daughter species in cometary comas have so far mostly been studied separately, as they require a different expertise: fluorescence of parent species is investigated by IR spectroscopy, while fluorescence of daughter species is investigated by UV-Vis spectroscopy. This segregation of parent and daughter species investigations hinders the comprehension of the chemistry of the comet coma as a whole, and by extension the chemistry of the comet nucleus. This work presents a first attempt to develop an expertise in IR spectroscopy in the Comet group of the STAR Institute of the University of Liège, already specialised in UV-Vis spectroscopy, with the end goal of making coordinated high resolution multi-wavelength observations of comets. It presents the development of PISCO (Pipeline for the Infrared Spectroscopy of COmets) and tests it with the data processing of a CRIRES 8P/Tuttle observation.

PISCO is a compilation of publicly available tools and home-made scripts. It goes through all the steps of comet IR data processing: image calibration and spectral extraction (with the ESO CRIRES pipeline), telluric and wavelength correction (with MOLECFIT), flux calibration, and finally retrieves the flux of individual lines to calculate the production rates and mixing ratios of the specie (with the intervention of PSG). It was build to maximise the synergy between the different tools used and reduce unnecessary user intervention. The functionality of some external tools was enhanced, e.g. by building a wrapper to facilitate the use of the most advanced functions of MOLECFIT, or creating a storage system allowing to reuse previous iterations of an optimisation. Some functionalities still need improvements. The flux calculation could be optimized to yield a more meaningful error on the flux values, and a fluorescence model still needs to be implemented to retrieve the production rates, which was not possible in the time frame of this work. However, a temporary solution using a model from PSG and rotational temperatures from the literature was used to present complete end results. Using external tools as part of PISCO proved to be problematic while they were not performing as expected and not enough documented, but as the problem could

finally be circumvented, the gain of not having to develop those complex tools is certainly welcome and allowed to bring PISCO to a more mature stage.

The reduction of 8P/Tuttle H_2O and the HCN datasets, observed by Kobayashi et al. 2010, using PISCO shows encouraging results. Values of flux for individual lines and the global production rates agree with the work of Kobayashi et al. 2010, proving the capabilities of PISCO but also of the PSG workaround to calculate the production rates. C_2H_6 and CH_4 datasets processing did not give as good results. C_2H_6 flux and production rate were too high, presumably because flat field correction could not be applied since using only the one flat frame available induced too much noise in the extracted spectrum. CH_4 is not detected at all. Uncertainties and S/N ratio are globally more important than those of Kobayashi et al. 2010; possible causes and avenues for improvements are discussed in the text.

PISCO is still in development and this first practical demonstration of its capabilities highlights flaws that will be corrected, while already producing some consistent results. In the future, PISCO may help the Comet group at the University of Liège in addressing the deficiency of expertise in IR comet spectroscopy in Europe, as well as accomplishing simultaneous observations of parent and daughter species in comets coma. With the development of always more performing IR spectrometers by European institutions, such as CRIRES+ and METIS, the future of multi-wavelength comet spectroscopy looks bright.

Appendix A: emission line fits for flux calculations

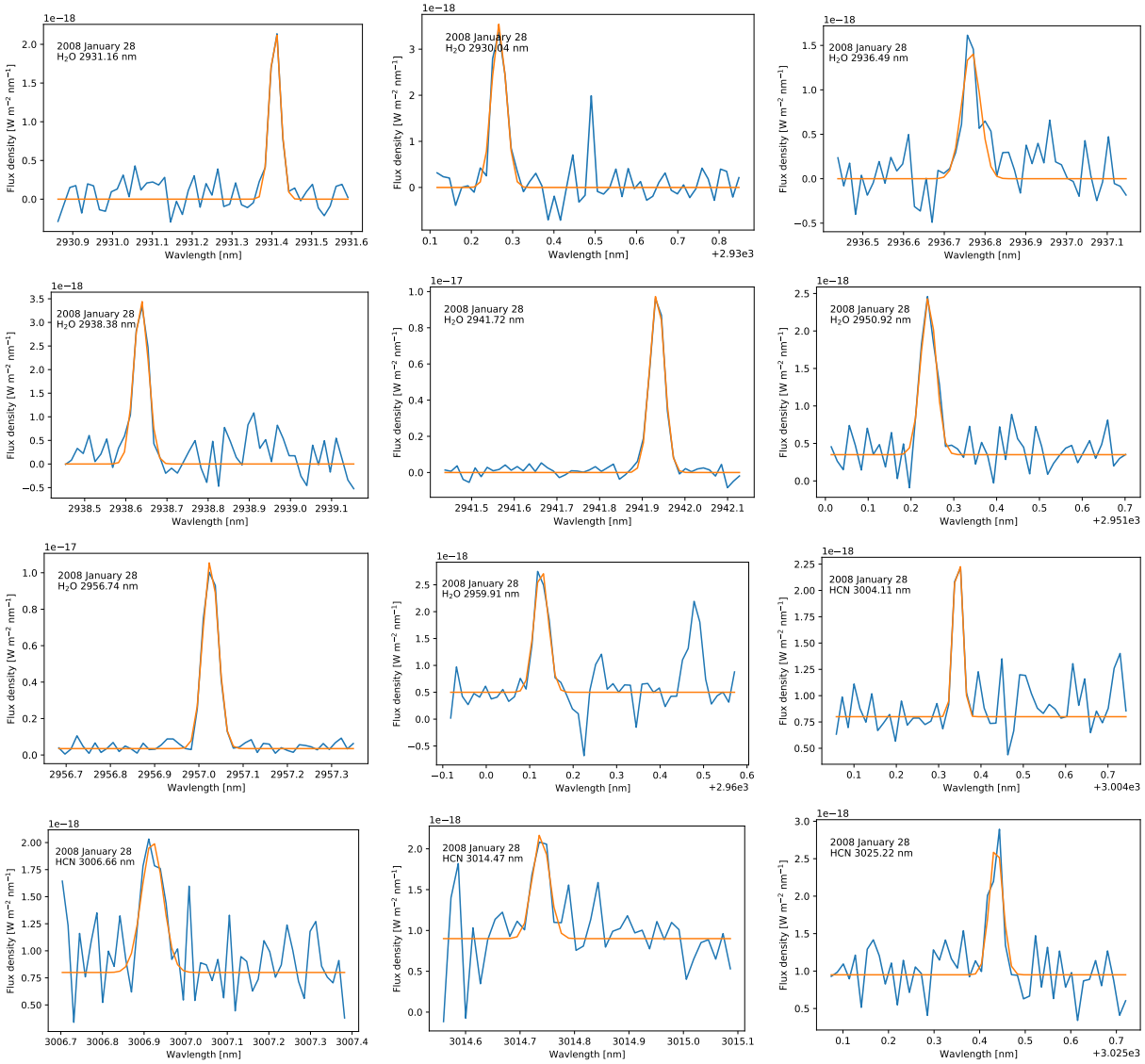

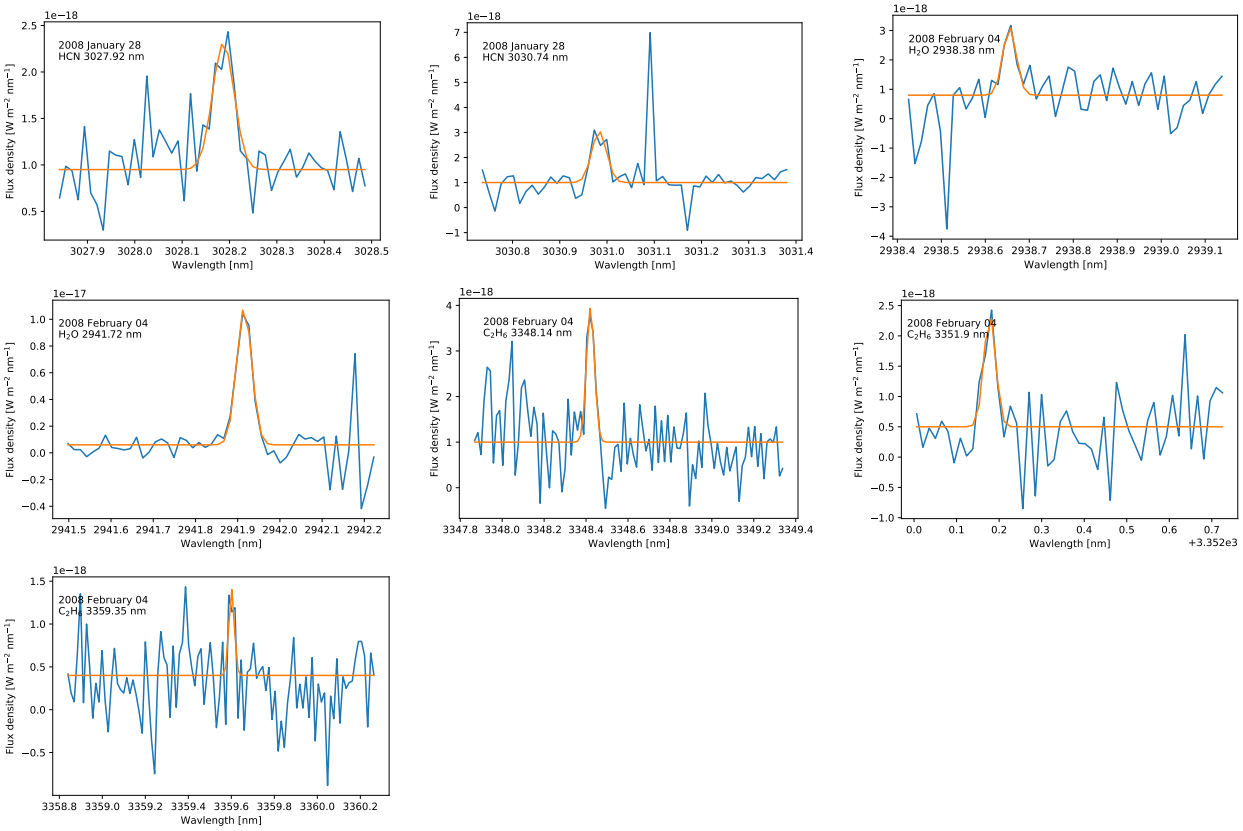
2008 January 28
HCN 3027.92 nm
2008 January 28
HCN 3030.74 nm
2008 February 04
H2O 2938.38 nm
2008 February 04
H2O 2941.72 nm
2008 February 04
C2H6 3348.14 nm
2008 February 04
C2H6 3351.9 nm
2008 February 04
C2H6 3359.35 nm
Flux density [W m−2 nm−1]
Wavlength [nm]
1e−18
1e−17
+3.352e3

References

A'Hearn, Michael F. et al. (Dec. 1995). "The Ensemble Properties of Comets: Results from Narrowband Photometry of 85 Comets, 1976-1992". en. In: *Icarus* 118.2, pp. 223–270. DOI: 10.1006/icar.1995.1190.

Altwegg, K. et al. (Jan. 2015). "67P/Churyumov-Gerasimenko, a Jupiter family comet with a high D/H ratio". en. In: *Science* 347.6220, pp. 1261952–1261952. DOI: 10.1126/science.1261952.

Altwegg et al. (2016). "Prebiotic chemicals—amino acid and phosphorus—in the coma of comet 67P/Churyumov-Gerasimenko". en. In: *Science Advances* 2.5, e1600285. DOI: 10.1126/sciadv.1600285.

Anders, Edward (1989). "Pre-biotic organic matter from comets and asteroids". In: *Nature* 342, pp. 255–257.

Asphaug, Erik and Willy Benz (June 1996). "Size, density, and structure of comet Shoemaker - Levy 9 inferred from the physics of tidal breakup". English (US). In: *Icarus* 121.2. Publisher: Academic Press Inc., pp. 225–248. DOI: 10.1006/icar.1996.0083.

Banwell, C. N. (1983). *Fundamentals of molecular spectroscopy*. 3rd ed. London ; New York: McGraw-Hill.

Biver, N. et al. (Oct. 1999). "Spectroscopic Monitoring of Comet C/1996 B2 (Hyakutake) with the JCMT and IRAM Radio Telescopes". In: *The Astronomical Journal* 118.4, pp. 1850–1872. DOI: 10.1086/301033.

Bockelée-Morvan, D et al. (2004). "The Composition of Cometary Volatiles". en. In: *Comets II*. Edited by Festou, M. C., Keller, H. U., and Weaver, H. A., The University of Arizona Press, Tucson, Arizona, p. 34.

Bockelée-Morvan, D. and N. Biver (July 2017). "The composition of cometary ices". en. In: *Philosophical Transactions of the Royal Society A: Mathematical, Physical and Engineering Sciences* 375.2097, p. 20160252. DOI: 10.1098/rsta.2016.0252.

Böhnhardt, H. et al. (Aug. 2008). "The Unusual Volatile Composition of the Halley-Type Comet 8P/Tuttle: Addressing the Existence of an Inner Oort Cloud". en. In: *The Astrophysical Journal* 683.1, pp. L71–L74. DOI: 10.1086/591446.

Bonev (2005). "Towards a Chemical Taxonomy of Comets: Infrared Spectroscopic Methods for Quantitative Measurements of Cometary Water (With an Independent Chapter on Mars Polar Science)". en. PhD thesis. University of Toledo.

Bonev et al. (June 2008). "The Peculiar Volatile Composition of Comet 8P/Tuttle: A Contact Binary of Chemically Distinct Cometesimals?" en. In: *The Astrophysical Journal* 680.1, pp. L61–L64. DOI: 10.1086/589649.

Brahe (1578). "Manuscript (in German). Codex Vind. 10689. (Translated in 1986 by J. Brager and N. Henningsen, E. Eilert- sen Publ., Copenhagen.)" In:

Brandl, Bernhard et al. (2021). "METIS: The Mid-infrared ELT Imager and Spectrograph". en. In: *Published in The Messenger vol. 182* pp. 22-26. Artwork Size: 5 pages Medium: PDF Publisher: European Southern Observatory (ESO), 5 pages. DOI: 10.18727/0722-6691/5218.

Ceccarelli, Cecilia et al. (2014). "Deuterium Fractionation: the Ariadne's Thread from the Pre-collapse Phase to Meteorites and Comets today". en. In: *arXiv:1403.7143 [astro-ph]*. arXiv: 1403.7143. DOI: 10.2458/azu_uapress_9780816531240-ch037.

Clough, S.A. et al. (Mar. 2005). "Atmospheric radiative transfer modeling: a summary of the AER codes". en. In: *Journal of Quantitative Spectroscopy and Radiative Transfer* 91.2, pp. 233–244. DOI: 10.1016/j.jqsrt.2004.05.058.

Cochran, A. L., E. S. Barker, and C. L. Gray (Mar. 2012). "Thirty years of cometary spectroscopy from McDonald Observatory". en. In: *Icarus* 218.1, pp. 144–168. DOI: 10.1016/j.icarus.2011.12.010.

Cohen, Martin et al. (Oct. 1992). "Spectral irradiance calibration in the infrared. I - Ground-based and IRAS broadband calibrations". en. In: *The Astronomical Journal* 104, p. 1650. DOI: 10.1086/116349.

Cremonese, G. et al. (Dec. 1997). "Neutral Sodium from Comet Hale-Bopp: A Third Type of Tail". en. In: *The Astrophysical Journal* 490.2, pp. L199–L202. DOI: 10.1086/311040.

Dorn, Reinhold J et al. (2014). "CRIRES+: Exploring the Cold Universe at High Spectral Resolution". en. In: p. 5.

Edgeworth, K. E. (Oct. 1949). "The Origin and Evolution of the Solar System". en. In: *Monthly Notices of the Royal Astronomical Society* 109.5, pp. 600–609. DOI: 10.1093/mnras/109.5.600.

Eicher, David J (2013). *Comets!: Visitors from Deep Space*. en. Cambridge University Press.

Elsila, Glavin, and Dworkin (2009). "Cometary glycine detected in samples returned by Stardust". In: *Meteoritics and Planetary Science* 44, pp. 1323–1330. DOI: 10.1111/j.1945-5100.2009.tb01224.x.

Festou, Keller, and Weaver (2004). "A brief conceptual history of cometary science". In: *Comets II*.

Glavin, Dworkin, and Sandford (2008). "Detection of cometary amines in samples returned by Stardust". en. In: *Meteoritics & Planetary Science* 43.1-2. _eprint: https://onlinelibrary.wiley.com/doi/p 5100.2008.tb00629.x, pp. 399–413. DOI: https://doi.org/10.1111/j.1945-5100.2008.tb00629.x.

Gomes, R. et al. (May 2005). "Origin of the cataclysmic Late Heavy Bombardment period of the terrestrial planets". en. In: *Nature* 435.7041, pp. 466–469. DOI: 10.1038/nature03676.

Halley (1705). *Astronomiae Cometicae Synopsis*. Oxford.

Haser (1957). "Distribution d'intensité dans la tête d'une comète". In: *Bull. Acad. R. Sci. Liège* 43, pp. 740–750.

Hill, Christian et al. (July 2016). "HITRANonline: An online interface and the flexible representation of spectroscopic data in the HITRAN database". en. In: *Journal of Quantitative Spectroscopy and Radiative Transfer* 177, pp. 4–14. DOI: 10.1016/j.jqsrt.2015.12.012.

Ho, Peng Yoke (Jan. 1962). "Ancient and mediaeval observations of comets and novae in Chinese sources". en. In: *Vistas in Astronomy* 5, pp. 127–225. DOI: 10.1016/0083-6656(62)90007-7.

Hollas, J. Michael (2004). *Modern spectroscopy*. en. 4th ed. Chichester ; Hoboken, NJ: J. Wiley.

Jehin, E. et al. (Sept. 2009). "A Multi-Wavelength Simultaneous Study of the Composition of the Halley Family Comet 8P/Tuttle". en. In: *Earth, Moon, and Planets* 105.2-4, pp. 343–349. DOI: 10.1007/s11038-009-9317-8.

Jewitt, David (Mar. 2012). "THE ACTIVE ASTEROIDS". en. In: *The Astronomical Journal* 143.3, p. 66. DOI: 10.1088/0004-6256/143/3/66.

Jewitt, David and Jane Luu (Apr. 1993). "Discovery of the candidate Kuiper belt object 1992 QB1". en. In: *Nature* 362.6422, pp. 730–732. DOI: 10.1038/362730a0.

Kaufl, Hans Ulrich et al. (2004). "CRIRES: A High Resolution Infrared Spectrograph for ESO's VLT". en. In: *Proceedings SPIE 5492*. Glasgow, United Kingdom, p. 10.

Kausch, W. et al. (Apr. 2015). "Molecfit: A general tool for telluric absorption correction - II. Quantitative evaluation on ESO-VLT/X-Shooterspectra". en. In: *Astronomy & Astrophysics* 576. Publisher: EDP Sciences, A78. DOI: 10.1051/0004-6361/201423909.

Kobayashi, H. et al. (Jan. 2010). "High-dispersion infrared spectroscopic observations of comet 8P/Tuttle with VLT/CRIRES ," en. In: *Astronomy and Astrophysics* 509, A80. DOI: 10.1051/0004-6361/200912477.

Kronk, Gary W., Maik Meyer, and David A. J. Seargent (1999). *Cometography: a catalog of comets*. Cambridge ; New York: Cambridge University Press.

Kuiper, G. P. (Jan. 1951). "On the Origin of the Solar System". en. In: *Proceedings of the National Academy of Sciences* 37.1, pp. 1–14. DOI: 10.1073/pnas.37.1.1.

Levison (1996). "Comet Taxonomy". In: vol. 107. T.W. Rettig and J.M. Hahn, Eds., pp. 173–191.

Lippi, Manuela (2010). "The composition of cometary ices asinferred from measured productionrates of volatiles". en. PhD thesis. Technischen Universität Carolo-Wilhelmina.

McQuarrie, Donald A. (2008). *Quantum chemistry*. en. 2nd ed. OCLC: ocn141484672. Sausalito, Calif: University Science Books.

MOLECFIT Pipeline team (Feb. 2021). *MOLECFIT Pipeline User Manual v4.1*. Available at www.eso.org.

Moorwood, Alan F. M. et al. (Mar. 2003). "CRIRES: a high-resolution infrared spectrograph for the VLT". In: *Proceedings SPIE 4841*. Ed. by Masanori Iye and Alan F. M. Moorwood. Waikoloa, Hawai'i, United States, p. 1592. DOI: 10.1117/12.457987.

Morbidelli, A and H Levison (2003). "Kuiper-belt interlopers". In: *Nature* 422, pp. 30–31. DOI: https://doi.org/10.1038/422030a.

Moulane, Youssef (2021). "Monitoring the activity and composition of comets with TRAPPIST telescopes". en. PhD thesis. Cadi Ayyad University, University of Liège.

Newburn, R. L., M. Neugebauer, and Jürgen H. Rahe, eds. (1991). *Comets in the Post-Halley Era*. en. Astrophysics and Space Science Library. Springer Netherlands.

Newton (1687). *Philosophiæ Naturalis Principia Mathematica*. Jussu Societalis Regiae ac typis Josephi Streatti. London.

Oliva, E. et al. (July 2014). "Concept and optical design of the cross-disperser module for CRIRES+". en. In: *Proceedings SPIE 9147*. Ed. by Suzanne K. Ramsay, Ian S. McLean, and Hideki Takami. Montréal, Quebec, Canada, 91477R. DOI: 10.1117/12.2054381.

Oort (1950). "The structure of the cloud of comets surrounding the Solar System and a hypothesis concerning its origin". In: *Communications from the observatory at Leiden* XI.408.

Opitom, Cyrielle (2016). "MONITORING OF THE CHEMICAL COMPOSITION OF COMETS IN THE FRAMEWORK OF THE TRAPPIST SURVEY". PhD thesis. University of Liège.

Quirico, E. et al. (July 2016). "Refractory and semi-volatile organics at the surface of comet 67P/Churyumov-Gerasimenko: Insights from the VIRTIS/Rosetta imaging spectrometer". en. In: *Icarus* 272, pp. 32–47. DOI: 10.1016/j.icarus.2016.02.028.

Rothman, L.S. et al. (June 2009). "The HITRAN 2008 molecular spectroscopic database". en. In: *Journal of Quantitative Spectroscopy and Radiative Transfer* 110.9-10, pp. 533–572. DOI: 10.1016/j.jqsrt.2009.02.013.

Sandford (2008). "Terrestrial Analysis of the Organic Component of Comet Dust". en. In: *Annual Review of Analytical Chemistry* 1.1, pp. 549–578. DOI: 10.1146/annurev.anchem.1.031207.113108.

Scheicher, D and A Bair (2014). "Chemical and physical properties of comets in the Lowell database: Results from 35 years of narrow-band photometry". In: Helsinki, Finland: K. Muinonen et al.

Smette, A. et al. (Apr. 2015). "Molecfit: A general tool for telluric absorption correction - I. Method and application to ESO instruments". en. In: *Astronomy & Astrophysics* 576. Publisher: EDP Sciences, A77. DOI: 10.1051/0004-6361/201423932.

Smoker, J (Dec. 2014). *CRIRES User Manual v92.3*. Available at www.eso.org.

Smoker, J et al. (Dec. 2013). *CRIRES data reduction cookbook v93.2*. Available at www.eso.org.

Stern, S A et al. (2019). "OVERVIEW OF INITIAL RESULTS FROM THE RECONNAISSANCE FLYBY OF A KUIPER BELT". en. In: *arXiv:1901.02578*, p. 3.

Swamy (2010). *Physics of comets*. en. 3rd ed. World Scientific series in astronomy and astrophysics v. 2. New Jersey: World Scientific.

Tsiganis, K. et al. (May 2005). "Origin of the orbital architecture of the giant planets of the Solar System". en. In: *Nature* 435.7041. Bandiera_abtest: a Cg_type: Nature Research Journals Number: 7041 Primary_atype: Research Publisher: Nature Publishing Group, pp. 459–461. DOI: 10.1038/nature03539.

Ueno, Yuichiro et al. (Mar. 2006). "Evidence from fluid inclusions for microbial methanogenesis in the early Archaean era". en. In: *Nature* 440.7083, pp. 516–519. DOI: 10.1038/nature04584.

Ulmer-Moll, S. et al. (Jan. 2019). "Telluric correction in the near-infrared: Standard star or synthetic transmission?" en. In: *Astronomy & Astrophysics* 621, A79. DOI: 10.1051/0004-6361/201833282.

Villanueva, G.L., K. Magee-Sauer, and M.J. Mumma (Nov. 2013). "Modeling of nitrogen compounds in cometary atmospheres: Fluorescence models of ammonia (NH3), hydrogen cyanide (HCN), hydrogen isocyanide (HNC) and cyanoacetylene (HC3N)". en. In: *Journal of Quantitative Spectroscopy and Radiative Transfer* 129, pp. 158–168. DOI: 10.1016/j.jqsrt.2013.06.010.

Villanueva, G.L., M.J. Mumma, et al. (Feb. 2012). "Water in planetary and cometary atmospheres: H2O/HDO transmittance and fluorescence models". en. In: *Journal of Quantitative Spectroscopy and Radiative Transfer* 113.3, pp. 202–220. DOI: 10.1016/j.jqsrt.2011.11.001.

Villanueva, G.L., M.D. Smith, et al. (Sept. 2018). "Planetary Spectrum Generator: An accurate online radiative transfer suite for atmospheres, comets, small bodies and exoplanets". en. In: *Journal of Quantitative Spectroscopy and Radiative Transfer* 217, pp. 86–104. DOI: 10.1016/j.jqsrt.2018.05.023.

Weidenschilling (2004). "From Icy Grains to Comets". In: *Comet II*.

Weissman, Paul R, Erik Asphaug, and Stephen C Lowry (2004). "Structure and Density of Cometary Nuclei". en. In: *Comets II*, p. 22.

Weissman, Paul R. (Mar. 1986). "Are cometary nuclei primordial rubble piles?" en. In: *Nature* 320.6059. Bandiera_abtest: a Cg_type: Nature Research Journals Number: 6059 Primary_atype: Research Publisher: Nature Publishing Group, pp. 242–244. DOI: 10.1038/320242a0.

Whipple, F. L. (Mar. 1950). "A comet model. I. The acceleration of Comet Encke". en. In: *The Astrophysical Journal* 111, p. 375. DOI: 10.1086/145272.

Yeomans, Donald K. (1991). *Comets: a chronological history of observation, science, myth, and folklore*. Wiley science editions. New York: Wiley.